

# Ce ions surface-modified TiO<sub>2</sub> aerogel powders: a comprehensive study of their excellent photocatalytic efficiency in organic pollutants removal

Received 00th January 20xx,  
Accepted 00th January 20xx

DOI: 10.1039/x0xx00000x

Guru Karthikeyan Thirunavukkarasu,<sup>a</sup> Olivier Monfort,<sup>a,\*</sup> Martin Motola,<sup>a</sup> Monika Motlochová,<sup>b</sup> Maroš Gregor,<sup>c</sup> Tomáš Roch,<sup>c</sup> Maria Čaplovicová,<sup>d</sup> Aleksandra Y. Lavrikova,<sup>e</sup> Karol Hensel,<sup>e</sup> Vlasta Brezová,<sup>f</sup> Monika Jerigová,<sup>g,h</sup> Ján Šubrt,<sup>b</sup> Gustáv Plesch<sup>a</sup>

Titanium dioxide aerogel (TiAP) powders were prepared by lyophilization of peroxo-polytitanic gels followed by annealing at 800 °C to obtain anatase structure. The surface modification of TiAP was performed for the first time by low extents of Ce ions (in the range from 0.0025 to 0.025 wt%) using a wet impregnation method. Photocatalytic activity of the aerogel samples was investigated in the removal of different organic pollutants (i.e., Rhodamine B, phenol and caffeine) and compared to the reference P25. Both TiAP and Ce ions surface-modified TiAP (Ce/TiAP) have exhibited better degradation efficiencies of pollutants than P25, especially for Ce/TiAP with an enhancement of +18 % and +37 % in the removal of caffeine and Rhodamine B, respectively. These results have been partly explained by the high active surface area of Ce/TiAP compared to TiAP as well as its better photo-electrochemical properties which have shown, for instance, ~10 % increased incident photon-to-electron conversion efficiency at 360 nm. Interestingly, the energetic position of the valence band maximum of Ce/TiAP is shifted from 3.2 eV to 2.8 eV (compared to TiAP), thus improving the generation of reactive oxygen species (ROS), especially hydroxyl radicals. Indeed, the presence of HO<sup>•</sup> is confirmed by electron paramagnetic resonance, and fluorescence spectroscopy and their photo-induced generation are enhanced in the case of Ce/TiAP. Finally, the surface modification of TiAP by cerium ions led to better photo-induced properties, thus limiting the electron-hole pair recombination, but also to the improvement of ROS generation via different plausible mechanisms.

## Introduction

Hazardous pollutants such as dyes, pesticides and pharmaceutical compounds, which are predominantly emitted by industrial activities, are the main source of contamination in the water bodies<sup>1–4</sup>. Concerning the treatment of wastewaters, several technologies including physical, chemical and biological, have been coupled to purify water<sup>5–7</sup>. Although the current technologies are efficient to some extent, there is still intense research to improve these treatments in order to limit the generation of other wastes and to decrease the costs

<sup>5,8</sup>. In addition, the environment agencies around the World have imposed stringent norms, especially in the European Union with the directives 91/271/CEE and 2008/105/CE on water quality and pollution control. Among the strategies to reach both efficient pollutants removal and sustainability, photochemical processes like photocatalysis are promising techniques since they can utilize sunlight to produce reactive oxygen species (ROS) able to decompose harmless pollutants to non-toxic byproducts<sup>7–9</sup>. As photocatalyst, titanium dioxide (TiO<sub>2</sub>) is widely investigated due to long-term stability, strong oxidizing power, non-toxicity and low cost<sup>8</sup>. Among different nanostructured TiO<sub>2</sub> materials (e.g., nanotubes, nanorods, nanopowders), TiO<sub>2</sub> aerogels exhibit high surface area, porosity and high contents of anatase phase<sup>10–13</sup>, thus leading to improved photocatalytic efficiency in the removal of organic pollutants<sup>14,15,13</sup>. The mechanism of TiO<sub>2</sub> photocatalysis is based on the generation of e<sup>-</sup>/h<sup>+</sup> pairs under suitable light irradiation ( $h\nu \geq E_g$ , i.e.  $\lambda \leq 390$  nm), and subsequent formation of ROS that decomposes the pollutants<sup>16,17,9</sup>. However, due to the relatively large energy bandgap of TiO<sub>2</sub> ( $E_g = \sim 3.2$  for the anatase phase), only UVA light can generate e<sup>-</sup>/h<sup>+</sup> pairs. Moreover, the fast e<sup>-</sup>/h<sup>+</sup> pair recombination rate in TiO<sub>2</sub> reduces its photocatalytic efficiency<sup>16–18</sup>.

To enhance the photocatalytic activity of TiO<sub>2</sub>, modification with metal/non-metal (F, C, N, Fe, Cu, Mn, etc.)<sup>19,20</sup> is reported to increase the incident light utilization, reduce e<sup>-</sup>/h<sup>+</sup> pair recombination, which in turn effectively increases the quantum yield, i.e. the photocatalytic efficiency<sup>21,22</sup>. Based on previous reports<sup>23,24,22</sup>, crystalline structure and morphology, optical and electronic properties of TiO<sub>2</sub> can be

<sup>a</sup> Department of Inorganic Chemistry, Faculty of Natural Sciences, Comenius University in Bratislava, Ilkovicova 6, Mlynska Dolina, 842 15 Bratislava, Slovakia

<sup>b</sup> Institute of Inorganic Chemistry, Czech Academy of Sciences, Husinec-Rez c.p. 1001, 250 68 Rez, Czechia

<sup>c</sup> Department of Experiment Physics, Faculty of Mathematics, Physics and Informatics, Comenius University in Bratislava, Mlynska Dolina, 842 48 Bratislava, Slovakia

<sup>d</sup> STU Center for Nanodiagnosics, Slovak University of Technology in Bratislava, Vazovova 5, 812 43 Bratislava, Slovakia

<sup>e</sup> Division of Environmental Physics, Faculty of Mathematics, Physics and Informatics, Comenius University in Bratislava, Mlynska Dolina, 842 48 Bratislava, Slovakia

<sup>f</sup> Institute of Physical Chemistry and Chemical Physics, Faculty of Chemistry and Food technology, Slovak University of Technology in Bratislava, Radlinskeho 9, 812 37 Bratislava, Slovakia

<sup>g</sup> International Laser Centre, Ilkovicova 3, 842 48 Bratislava, Slovakia

<sup>h</sup> Department of Physical and Theoretical Chemistry, Faculty of Natural Sciences, Comenius University in Bratislava, Ilkovicova 6, Mlynska dolina, 842 15 Bratislava, Slovakia

\* Corresponding author: monfort1@uniba.sk (email), +421(0)290142141 (phone)  
Electronic Supplementary Information (ESI) available: See  
DOI: 10.1039/x0xx00000x

modified/adjusted by rare earth metals (Eu, La, Sc, Y, etc.). Among the rare earth metals, Ce possesses interconvertible oxidation states ( $\text{Ce}^{3+}/\text{Ce}^{4+}$ ) resulting in (i) the varying oxygen concentration in the lattice, (ii) increasing the active surface sites, (iii) altering the band position, and (iv) suppressing the grain growth of  $\text{TiO}_2$ <sup>8,25–27</sup>. Additionally, Ce can activate *in-situ* photo-generated  $\text{H}_2\text{O}_2$ , thus leading to increased ROS generation<sup>72</sup>. However, an excess of Ce hinders the photocatalytic efficiency of  $\text{TiO}_2$ <sup>26</sup>. Indeed, excess Ce ions acts as recombination centers for  $e^-/h^+$  pairs<sup>28–31,26</sup>. Therefore, it appears crucial to modify  $\text{TiO}_2$  (i) with the low amount of Ce ions and (ii) preferentially at the surface of the material since photocatalysis follows the Langmuir-Hinshelwood mechanism<sup>32,33</sup> (i.e., it proceeds at the photocatalyst/pollutant interface). An overview of some important works on Ce-modified  $\text{TiO}_2$  is summarized in Table S1 (Electronic Supplementary Information). It is interesting that most of these published works are based on Ce doping, not surface modification. This is one of the reasons that has motivated us to study Ce ions surface modified  $\text{TiO}_2$  systems which are scarcely detailed in the literature.

On the other hand, the literature describing Ce ions as surface-modifier of  $\text{TiO}_2$  (and not as a dopant) is scarce. In this work, titanium dioxide aerogels (TiAP) were prepared by lyophilization (freeze-drying) of peroxo-polytitanic acid gels followed by annealing in air at 800 °C<sup>34,35</sup>. To the best of our knowledge, we report the surface modification of such TiAP powders by Ce ions for the first time. To this end, impregnation of a low amount of cerium (IV) ammonium nitrate solution (from 0.1 to 0.01 wt%, thus leading to Ce ions between 0.0025 and 0.025 wt%) was used. After a comprehensive physical, optical and photo-electrochemical characterization of the samples, we have thoroughly discussed the effect of cerium ions and provided new insights into the photocatalytic efficiency of surface-modified Ce/TiAP. The photocatalytic study involved the degradation of different types of relevant pollutants in water under solar-like irradiation (mostly UVA light). Indeed, as model pollutants, we have tested (i) Rhodamine B (RB) which is widely used as a colorant in textiles, and food industries but which has also proven to be carcinogenic, and toxic to both humans as well as animals<sup>36–38</sup>, (ii) phenol since its derivatives are non-biodegradable and possess acute toxicity to the aquatic environment<sup>5</sup>, and (iii) caffeine (CAF) which is a highly used psychoactive drug that has adverse negative effects on the environment<sup>39</sup>. These hazardous organic pollutants are easily detected and accumulated in the environment<sup>40–43</sup>. To further highlight the relevance of our study, the obtained results are compared with commercial Aeroxide P25 powders.

## Materials and methods

### Chemicals

Titanium (IV) oxysulfate ( $\text{TiOSO}_4 \cdot x\text{H}_2\text{O}$ , > 29 % Ti as  $\text{TiO}_2$ , Sigma-Aldrich) was used as a titanium precursor for the preparation of TiAP. Ammonia ( $\text{NH}_3$ , 25–29 %) and hydrogen peroxide (30 %  $\text{H}_2\text{O}_2$ ) were purchased from Penta s.r.o. (Slovakia). Cerium ammonium nitrate ( $\text{Ce}(\text{NH}_4)_2(\text{NO}_3)_6$ , 98+ %) was purchased from Alfa Aesar. Commercially available Aeroxide- $\text{TiO}_2$  P25 is used as a reference sample. Rhodamine B

(99+ %, Acros Organics), caffeine (ReagentPlus®, Sigma Aldrich), and phenol (99.0 %, CentralChem, Slovakia) were used as model organic pollutants. Terephthalic acid and hydroxy-terephthalic acid (used in the assessment of  $\text{HO}^\bullet$  radical) were purchased from Sigma-Aldrich. Ammonium oxalate monohydrate (99+ %, Acros Organics) and 1,4 benzoquinone (99.0 %, Acros Organics) were used for radical scavenging experiments.

### Synthesis of TiAP and Ce/TiAP

The titanium dioxide aerogel powders (TiAP) are prepared by freeze-drying and subsequent annealing of peroxo-polytitanic acid gel according to previous reports<sup>34,35</sup>. Briefly, titanium oxysulfate solution (0.2 M) was prepared at 35 °C under constant stirring. After, the solution was cooled down to 0 °C followed by addition of ammonia until it reached  $\text{pH} = 8$ , thus resulting in the formation of white precipitate. The precipitate was filtered and washed at ambient temperature. After several steps of resuspension, decantation and washing, the product was suspended in 350 mL of distilled water followed by the addition of  $\text{H}_2\text{O}_2$  until the  $\text{pH}$  was in the range of 1–2. The suspension was stirred at room temperature for about 30 min until a clear transparent yellow solution was formed. Afterwards, the yellow solution was sprayed into liquid  $\text{N}_2$  and subsequently lyophilized using a freeze dryer at a temperature of –64 °C and pressure of 5–10 mTorr. The obtained yellow foamy aerogel was annealed at 800 °C for 2 h to form TiAP.

The cerium ions modified titanium dioxide aerogel powders (Ce/TiAP) were prepared through the wet impregnation method. Firstly, TiAP suspension was prepared using distilled water (100 mg in 100 mL). Secondly, the TiAP suspension was mixed with 0.1 mL of Cerium ammonium nitrate precursor solution (1.0, 0.5, 0.1  $\text{mg}\cdot\text{mL}^{-1}$ , respectively) and kept under stirring for 1 h to obtain Ce/TiAP with different concentrations of Ce ions (0.025, 0.0125, 0.0025 wt%, respectively). Thirdly, the mixture was centrifuged, and the collected Ce/TiAP was dried at 80 °C for 2 h. Finally, both TiAP and Ce/TiAP were annealed in air at 800 °C for 2 h to obtain crystalline anatase structure. The nominal amount of Ce in the surface-modified TiAP ranges from 0.025 to 0.0025 wt%, which corresponds to the range  $1.5 \cdot 10^{-3}$  –  $1.5 \cdot 10^{-2}$  at%.

### Structural and optical characterization

The crystalline phase composition of all the samples was analyzed by X-ray diffraction using PANalytical X-ray diffractometer ( $\text{Cu } K_\alpha$  radiation,  $\lambda = 1.5418 \text{ \AA}$ ) in grazing incidence mode (GI-XRD). To investigate the morphology of the samples, and more particularly the surface, Transmission Electron Microscopy studies (TEM, JEOL JEM ARM 200cF, 200 kV) were performed. For TEM investigations, the powder samples were dispersed by sonication in ethanol for 5 min and loaded onto a holey carbon-coated Cu TEM grid. After drying in air, the samples were studied by TEM, High Resolution TEM (HRTEM), Selected Area Electron Diffraction (SAED), and Scanning TEM (STEM) methods. For detailed SEM images of the nanocrystals, STEM-SEI detector was used. Ultrascan CCD camera with resolution of  $2048 \times 2048$  pixels and the Digital Micrograph software package were used for taking and processing of images. To identify the presence of Ce in TiAP, Secondary Ion Mass Spectrometry (SIMS) was performed using

a reflectron type time-of-flight mass spectrometer (ToF-SIMS IV, ION-TOF, Germany) equipped with a bismuth ion source. Pulsed 25 keV Bi<sup>+</sup> were used as primary ions with a current of 1 pA with total primary ion dose density below the static limit of 10<sup>13</sup> ions·cm<sup>-2</sup>. Secondary ion mass spectra were measured by scanning over a selected 100 × 100 μm<sup>2</sup> analysis area. The active surface area, pore diameter and pore volume was measured by N<sub>2</sub> adsorption-desorption isotherm at -196 °C using a Quantachrome Nova 4200e instrument. Prior to the measurement, the samples were outgassed for 48 h at 23 °C. The specific surface area was calculated by the BET (Brunauer, Emmett, Teller) method and pore diameter and pore volume were calculated using a cylindrical pore model (BJH)<sup>44,45</sup>. To investigate the optical properties of TiAP and Ce/TiAP, diffuse reflectance spectroscopy (DRS) was used in the wavelength range from 300 to 800 nm using Ocean Optics USB650 UV spectrometer equipped with an optical fibre (R200-7-SR) using a deuterium and tungsten halogen lamp as the light sources. The Kubelka-Munk function and Tauc's plot were then used to determine the optical energy bandgap ( $E_g$ ) of TiAP and Ce/TiAP. The valence band maximum (VBM) was measured using Ultraviolet Photoelectron Spectroscopy (UPS) using Omicron multi-probe system with photons of energy: He(I) = 21.2 eV.

#### Photo-electrochemical measurements

Prior to photo-electrochemical measurements, the samples were drop coated as a thin layer on Ti foil (1.5 cm × 1.5 cm) followed by annealing at 300 °C for 2 h<sup>46</sup>. The photocurrent measurements were carried out in a three-electrode cell using Ag/AgCl as a reference electrode, Pt wire as a counter electrode and the photoactive layer as a working electrode at 0.4 V vs. Ag/AgCl in an aqueous 0.1 M Na<sub>2</sub>SO<sub>4</sub> solution in the spectral range from 300 nm to 500 nm. A photoelectric spectrophotometer (Instytut Fotonowy) with a 150 W Xe lamp and a monochromator with a bandwidth of 5 nm connected with a modular electrochemical system AUTOLAB (PGSTAT 204; MetrohmAutolab B. V.; Nova 1.10 software) was used for photocurrent measurements. The photocurrent transients were recorded under chopped light irradiation (light on/off cycles of 10 s). Cyclic voltammograms (CV) were recorded in the potential range from -0.4 V vs Ag/AgCl to +1.0 V vs. Ag/AgCl with a sweep rate of 5 mV·s<sup>-1</sup>, starting at 0 V towards positive voltages (three-times repeated voltammetry cycles) in the dark and under UV light irradiation ( $\lambda = 350$  nm), respectively.

#### Photocatalytic measurements

The photocatalytic activity of P25, TiAP and Ce/TiAP samples was investigated under solar-like irradiation for the degradation of different pollutants including Rhodamine B (10 ppm), caffeine (20 ppm) and phenol (20 ppm). The solar-like irradiation was generated by a metal-halogen arc-lamp (HQI TS – OSRAM 400W/D6500K) equipped with a pyrex glass filter to cut-off UVB irradiation. The intensity of UVA light in the wavelength range 335-380 nm was 1.3 mW·cm<sup>-2</sup>. In a typical procedure, a 30 mL pollutant solution containing 0.2 g·L<sup>-1</sup> of photoactive samples was kept in the dark for 30 min to reach the adsorption/desorption equilibrium. Then, during irradiation, the suspension was kept under constant magnetic stirring, and air bubbling and 2 mL samples were withdrawn at predetermined reaction time. Before analysis of the

degradation extent, each sample was centrifugated, and the collected supernatant was filtrated (0.45 μm PTFE filter).

In the case of RB degradation, only the decolorization was followed for 10 min irradiation time. To this end, degradation extent was determined by following the absorbance at 554 nm using UV-VIS spectrophotometer (Jasco V-530). In the case of CAF degradation, the degradation extent at predetermined reaction time was investigated using High-Performance Liquid Chromatography (HPLC, Nexera LC-20AD XR) equipped with C18 column (Agilent) and diode array detector (prominence SPD-M20A) set at 272 nm. The mobile phase was composed of a mixture of milli-Q water and acetonitrile (ACN) acidified by 0.1% H<sub>3</sub>PO<sub>4</sub> in gradient eluent mode (H<sub>2</sub>O/ACN from 80:20 to 20:80 reached in 6 min). The flow rate was 0.8 mL·min<sup>-1</sup>, and the injection volume was 25 μL. In addition, mineralization was monitored using total organic carbon analysis (TOC, Shimadzu TOC 5000A) as in the case of phenol degradation. For TOC analysis, longer irradiation time was used (2 h). Repeated runs of photocatalytic removal of RB, phenol and CAF have been performed without regeneration of the photocatalyst. For RB degradation, irradiation cycles are 10 min long while for phenol and CAF mineralization (analyzed by TOC), each cycle is 60 min long.

#### Study of photocatalytic mechanism

The generation of hydroxyl radicals (HO<sup>\*</sup>) under solar-like irradiation for P25, TiAP and Ce/TiAP was investigated by fluorescence spectroscopy (Shimadzu RF-6000). The experimental procedure involved the addition of titania powder into the terephthalate solution. Before UVA irradiation, the suspension was kept in the dark for 30 min. Upon irradiation, hydroxyl radicals reacted with terephthalate to form hydroxy terephthalate, which is a fluorescent compound ( $\lambda_{exc} = 310$  nm and  $\lambda_{em} = 425$  nm)<sup>47,48</sup>. To avoid light scattering by suspended particles, each sample was previously centrifugated before analysis of the supernatant. For quantification of photo-generated HO<sup>\*</sup>, a calibration curve was plotted using hydroxy terephthalate solution with concentration ranging from 0.1 μM to 0.1 mM. Further analysis of the presence of reactive oxygen species in the form of radicals was performed by electron paramagnetic resonance (EPR). The X-band cw-EPR spectra (modulation frequency of 100 kHz) were monitored with the EMXplus spectrometer (Bruker) equipped with the High Sensitivity Probe-head (Bruker) in the small quartz flat cell (Wilma-LabGlass, WG 808-Q). The suspensions prepared by mixing the corresponding stock solution/suspension in deionized water were irradiated at 295 K directly in the EPR resonator utilizing a LED@365 nm source ( $\lambda_{max} = 365$  nm; Bluepoint LED, Höhle UV Technology; irradiance 10 mW·cm<sup>-2</sup>). The EPR spectra were recorded in situ during/after a defined exposure. The spin trapping agents, *i.e.* 5,5-dimethyl-1-pyrroline *N*-oxide (DMPO, distilled and stored at -20 °C before the application; Sigma-Aldrich) and 5-*tert*-butoxycarbonyl-5-methyl-1-pyrroline *N*-oxide (BMPO, Enzo Life Sciences) were used. The spin trapping experiments were performed at least in triplicate. The *g*-factors were determined with an uncertainty of ±0.0001 exploiting a nuclear magnetic resonance teslameter (ER 036TM, Bruker) and integrated frequency counter. The experimental EPR spectra were analyzed by the WinEPR software (Bruker), and the calculations of spin-Hamiltonian

parameters and relative concentrations of individual BMPO-adducts were performed with the EasySpin toolbox working on MatLab® platform<sup>49</sup>. The standard EPR spectrometer settings were as follows: microwave frequency: ~9.43 GHz; microwave power: ~10.5 mW; centre field ~335.8 mT; sweep width 8 mT; gain 1.00×10<sup>5</sup>; modulation amplitude: 0.05 mT; sweep time: 18 s; time constant: 5.12 ms; the number of scans: 1 or 10. To corroborate EPR analyses, radical scavenging experiments were also performed using 10 mM isopropanol (IPA, HO• scavenger), 0.1 mM benzoquinone (BQ, O<sub>2</sub><sup>•-</sup> scavenger) and 2.0 mM ammonium oxalate (AO, h<sup>+</sup> scavenger).

## Results and discussion

Prior to the main experiments, the optimization of Ce content at the surface of TiAP was investigated. To this end, 0.00125, 0.0025, 0.0125 and 0.025 wt% of Ce/TiAP samples were prepared, and their photocatalytic efficiency in the decolorization of Rhodamine B was assessed (Figure S1 and Table S2). Based on these preparatory experiments, 0.0025 wt% Ce/TiAP showed the best photocatalytic activity, thus being further studied in the rest of this work.

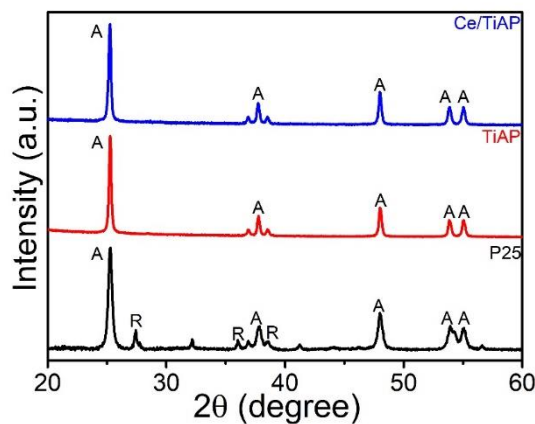


**Figure 1:** XRD patterns of P25, TiAP, and Ce/TiAP. The diffractions labelled A and R are assigned to Anatase and Rutile phase of TiO<sub>2</sub>.

### Morphology and structure of TiAP and Ce/TiAP

The XRD patterns of TiAP and Ce/TiAP along with the commercially available P25 powder are shown in Figure 1. For the P25 powder, both anatase (ICDD 03-065-5714) and rutile (ICDD 03-065-1118) TiO<sub>2</sub> phases were identified. Indeed, the 2θ diffractions at approx. 25.29, 37.72, 48.01, 52.80, and 55.04° correspond to (101), (004), (200), (105) and (211) TiO<sub>2</sub> anatase phase crystal structure, respectively. Wherein the TiO<sub>2</sub> rutile phase has 2θ diffractions at 27.40, 36.02 and 41.17° which correspond to (110), (101) and (111) diffraction planes, respectively. It is worth noting that P25 powder is composed of 82% of anatase and 18% of rutile (Electronic Supplementary Information). Solely anatase was detected in TiAP and Ce/TiAP. Regarding the preparation method of Ce/TiAP, it can be deduced that Ce is present at the surface of TiO<sub>2</sub>, probably in the form of CeO<sub>2</sub> nanocrystals. The average crystallite sizes for each sample were calculated using the Debye-Scherrer equation based on the full-width at half maximum (FWHM) of anatase TiO<sub>2</sub> (101) diffraction peak (equation 1)<sup>50</sup>.

$$D_{hkl} = \frac{K\lambda}{B_{hkl} \cos \theta} \quad (\text{eq. 1})$$

where  $D_{hkl}$  is the crystallite size,  $hkl$  is the Miller indices of the plane being analyzed,  $K$  is the crystallite-shape factor, which is approximated 0.9,  $\lambda$  is the wavelength of the X-rays,  $B_{hkl}$  is the FWHM of the X-ray diffraction peak in radians, and  $\theta$  is the Bragg angle. The calculated crystallite size of P25, TiAP and Ce/TiAP was approx. 20 nm, 32 nm and 29 nm, respectively. In general, TiAP possesses bigger crystallite size than P25. This is the result of the different methods used for the preparation of TiO<sub>2</sub>, namely flame pyrolysis (for P25) and freeze-drying (for TiAP). The freeze-drying process removes the aqueous component from the peroxy-polytitanic acid gel while preserving the porous structure in the dried state<sup>51</sup>. The freeze-drying helps the stability of TiO<sub>2</sub> anatase at high temperature since it prevents the formation of rutile nuclei. In addition, during the annealing procedure, the structure of peroxy-polytitanic acid gel prevents the transport of the material to the growing anatase phase, thus leading to the inhibition of the particle growth and assisting in the stabilization of TiO<sub>2</sub> anatase phase<sup>51–53</sup>. Concerning the two TiAP samples, Ce surface modification retards the growth of TiO<sub>2</sub> grain and thereby reducing the crystallite size of anatase TiO<sub>2</sub><sup>28,7</sup>. Since ionic radii of Ce<sup>3+</sup>/Ce<sup>4+</sup> ions (1.03/1.02 Å) is larger than that of Ti<sup>4+</sup> ions (0.68 Å), the resulting cerium species occupy space at grain boundaries and grain junctions rather than Ce ions replacing titanium sites in anatase lattice<sup>54</sup>. Therefore, the crystallite growth of TiO<sub>2</sub> is hindered through Ce-Ti-O bond formation<sup>54</sup>.

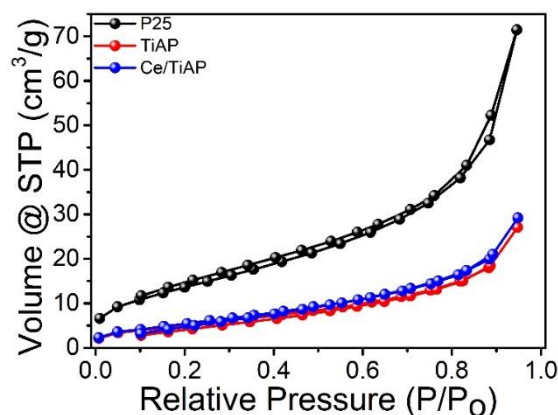


**Figure 2:** BET Adsorption-desorption isotherm of P25, TiAP and Ce/TiAP.

The Brunauer–Emmett–Teller (BET) adsorption/desorption isotherm of all samples was performed (Figure 2 and Figure S2), and the results are summarized in Table 1. It is confirmed that both TiAP and Ce/TiAP possess smaller surface area and pore volume compared to those of P25. However, the higher surface area of Ce/TiAP (17.3 m<sup>2</sup>·g<sup>-1</sup>) compared to that of TiAP (15.6 m<sup>2</sup>·g<sup>-1</sup>) can be explained by a successful surface modification of TiAP by Ce.

**Table 1:** Data from BET measurements on specific surface area ( $S_{\text{BET}}$ ), pore volume and average pore diameter.

Sample Name	$S_{\text{BET}}$ ( $\text{m}^2\cdot\text{g}^{-1}$ )	Pore Volume ( $\text{cm}^3\cdot\text{g}^{-1}$ )	Average Pore Diameter (nm)
P25	35.4	0.098	3.48
TiAP	15.6	0.040	3.50
Ce/TiAP	17.3	0.042	3.48

To correlate the BET data, the surface morphology of the  $\text{TiO}_2$  powder was investigated by STEM and TEM. STEM and low-mag TEM images with relevant SAED patterns of Ce/TiAP, TiAP, and P25 samples are shown in Figure 3. SAED patterns taken from randomly oriented crystallites in TiAP and Ce/TiAP consist of diffraction rings that can be ascribed exclusively to the tetragonal  $\text{TiO}_2$  anatase phase. In P25, along with diffraction rings assigned to anatase phase, there can be seen spots exhibiting interplane spacing of 0.32 nm which is the most intense reflection of tetragonal  $\text{TiO}_2$  rutile phase. These observations are consistent with the XRD measurements. It is

with an average size of 50 nm (as measured from TEM 2D projections), which is different from the values calculated by XRD. This discrepancy can be elucidated as follows: the crystallite size obtained by XRD is related to the smallest crystalline coherent domains forming individual nanocrystals and not to the size of the particles formed by oriented attachment of several nanocrystals with similar crystallographic orientations. Examples of the merged nanocrystals in TiAP and Ce/TiAP oriented in  $\langle 010 \rangle$  and  $\langle 111 \rangle$  directions are provided in Figure 4a and Figure 4c. As follows from the relevant FFT patterns (Figure 4b and Figure 4d), the  $\{101\}$  type surfaces are predominant, which indicates dipyrnidal morphology. Indeed, the anatase nanoparticles in Ce/TiAP and TiAP contain faceted truncated bipyramidal nanocavities (Figure 4a). To prove the presence of Ce in Ce/TiAP, SIMS analysis was performed (Figure S3). For consistency, SIMS was also performed on the other Ce/TiAP samples containing 0.0125 and 0.025 wt% of Ce in TiAP (Figure S3) and the intensity of  $\text{Ce}^+$  peak (at the mass of 139.9 u) increases with the increasing Ce concentration.

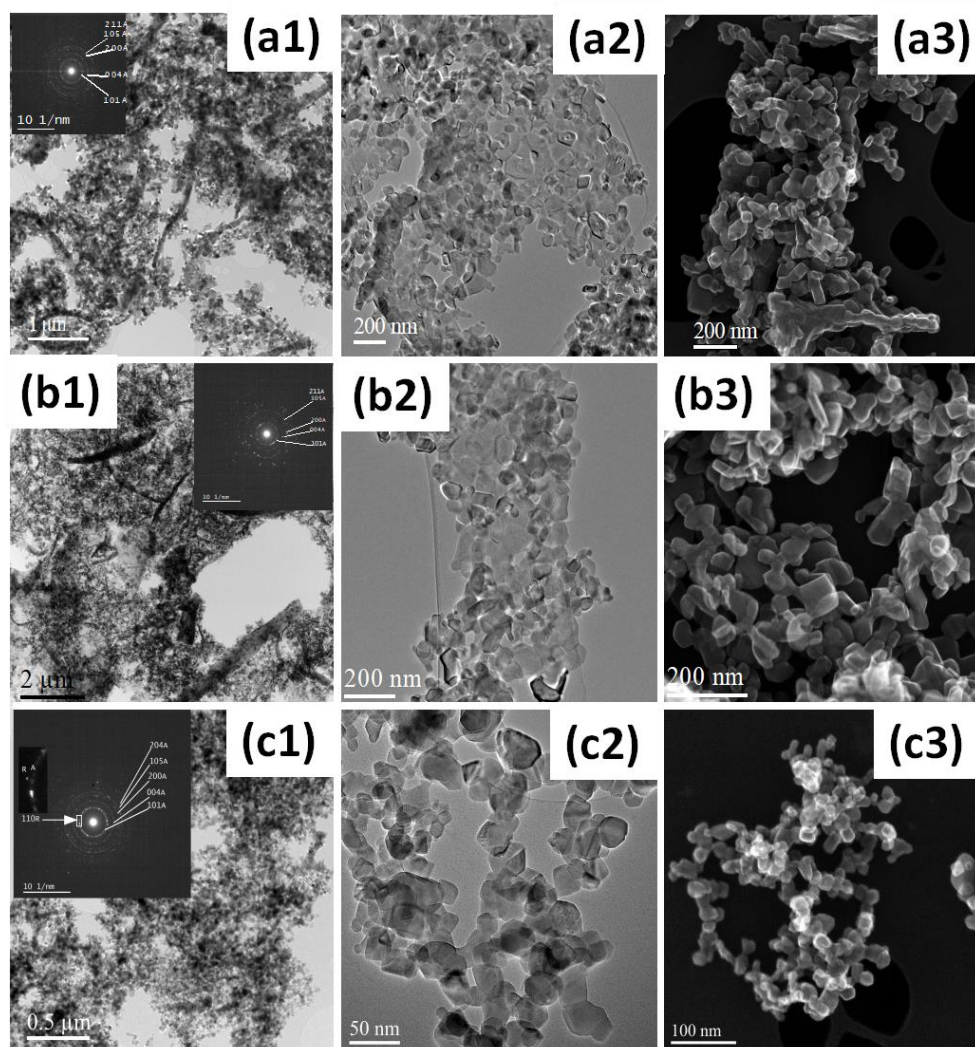


**Figure 3:** Low magnification TEM and SEM images of a) Ce/TiAP b) TiAP and c) P25.

worth noting that the low magnification TEM images shows that the nanoparticles in all the samples are aggregated (Figure 3). In addition, TiAP and Ce/TiAP exhibit 2D nanosheet, which is consistent with previous work<sup>51</sup>. The size of nanocrystals in Ce/TiAP and TiAP ranged from 20 to 110 nm

#### Optical properties of TiAP and Ce/TiAP

The optical properties of P25, TiAP and Ce/TiAP were investigated by DRS and UPS spectroscopies. The DRS spectra

showed that the peak reflectance of the TiAP and Ce/TiAP is shifted towards lower wavelengths compared to P25, from 405 nm to 395 nm (Figure 5a). This is due to the presence of rutile phase in P25 ( $E_g = \sim 3.0$  eV), thus contributing to slightly smaller  $E_g$  than TiAP and Ce/TiAP which contain only anatase ( $E_g = \sim 3.2$  eV)<sup>55-57</sup>. The optical bandgap ( $E_g$ ) calculated from Kubelka-Munk function (for the case of the indirect bandgap) and determined by the Tauc's plot (Figure 5b) exhibit that P25 has a bandgap of  $\sim 3.09$  eV while  $\sim 3.25$  eV for TiAP and Ce/TiAP. Therefore, no significant shift in optical bandgap between TiAP and Ce/TiAP is observed. This is in accordance with previous studies on TiO<sub>2</sub> aerogel powders surface-modified by Nd, Ag, and Au<sup>51</sup>. Nevertheless, from UPS spectra (Figure 6), the shift of the valence band maximum (VBM) towards lower values was recorded (from 3.2 eV to 2.8 eV for TiAP and Ce/TiAP, respectively). This shift of the electronic band structure in Ce/TiAP is beneficial for the generation of ROS.

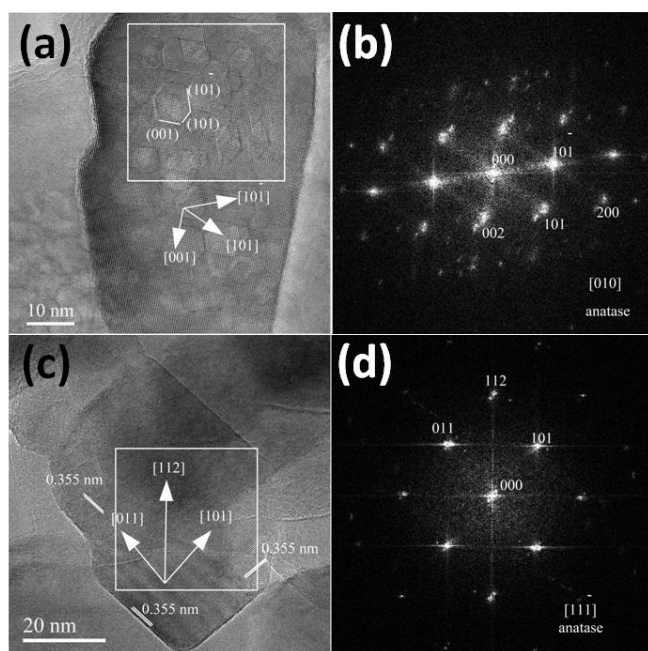


**Figure 4:** HRTEM of (a) anatase single crystal oriented in  $\langle 010 \rangle$  direction formed by oriented attachment (relevant FFT pattern in (b)), and (c) anatase single crystal oriented in  $\langle 111 \rangle$  direction formed by oriented attachment (relevant FFT pattern in (d)).

#### Photo-electrochemical characterization of TiAP and Ce/TiAP

The photocurrent densities and the recorded photocurrent transients from 250 nm to 500 nm are shown in ESI (Figure S4). Figure 7a show the corresponding (from Figure S4) incident photon-to-electron conversion efficiencies (IPCE) recorded for P25, TiAP, and Ce/TiAP in the wavelength range from 300 nm to 500 nm. A pronounced increase in the photocurrent density and IPCE was observed for TiAP and Ce/TiAP compared to P25. At the wavelength of  $\sim 350$  nm, the IPCE values reached approx. 50 %, 40 %, and 30 % for Ce/TiAP, TiAP, and P25, respectively. The  $\sim 10$  % increase in IPCE for TiAP compared to P25 is mainly due to the 2D-nanosheet morphology of the TiAP that have superior charge carrier mobility that also contributes to the increase in IPCE<sup>58-60</sup>. In Ce/TiAP, the IPCE value reached

$\sim 50\%$  at 350 nm. Indeed, Ce modification increases the incident light utilization and decreases the  $e^-/h^+$  recombination<sup>61,62</sup>. Figure 7b shows  $(IPCE \cdot hv)^{1/2}$  plots which were employed to evaluate the indirect bandgap energy of samples and are summarized in Table 2. Here, the bandgap values calculated for all the samples were  $\sim 3.13$  eV, that is similar to the evaluated optical bandgap results obtained from DRS (Figure 5).

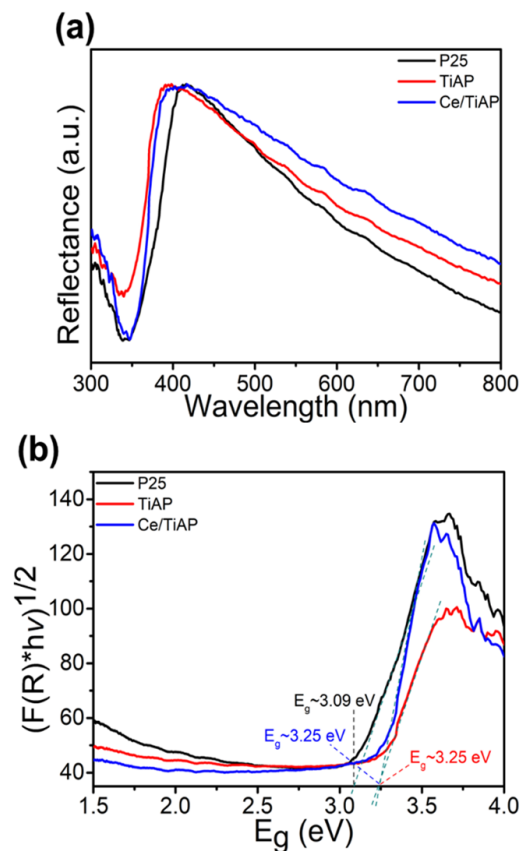


**Figure 5:** a) UV-DRS b) Tauc's plot of P25 sample, TiAP and Ce/TiAP.

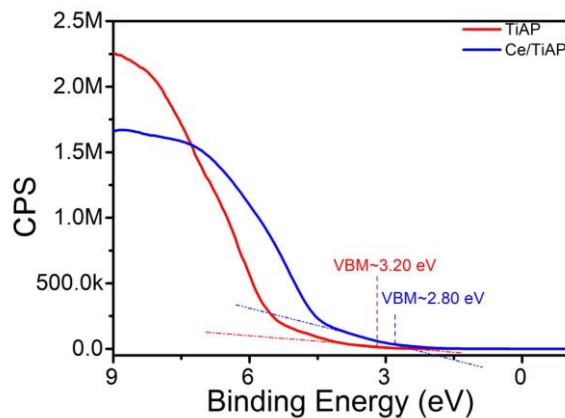


**Figure 6:** Ultraviolet Photoelectron Spectroscopy (UPS) spectra of TiAP and Ce/TiAP and the corresponding valence band maximum (VBM).

To provide an additional photo-electrochemical insight, cyclic voltammograms (CV) were recorded in the potential range from -0.4 V vs. Ag/AgCl to +1.0 V vs. Ag/AgCl for P25, TiAP, and Ce/TiAP. Figure 7c and 7d show CV curves recorded in the dark and under UV light irradiation ( $\lambda = 350$  nm), respectively. The CV shape for all samples is typical for the anatase structure<sup>63,64</sup>. The current density in the dark (Figure 7c) of Ce/TiAP increased in the potential range from approx. -0.2 V vs. Ag/AgCl to +0.2 V vs. Ag/AgCl due to Ce doping of TiAP. The dark currents of TiAP and P25 are almost identical. After UV light irradiation ( $\lambda = 350$  nm), a pronounced increase in photocurrent densities was observed for all samples. The recorded CVs are in correlation with the obtained photocurrent densities (Figure S4a) and IPCEs (Figure 7a). The photocurrent densities for all samples increased until the potential of approx. +0.4 V vs. Ag/AgCl. At higher potentials, a photocurrent plateau was observed, indicating that the thickness of the particles equals the space charge layer<sup>65,63,64</sup>.

observed photocatalytic degradation followed the pseudo-first-order kinetic based on the Langmuir-Hinshelwood kinetic model (equation 2)<sup>66</sup>,

$$kt = -\ln\left(\frac{C}{C_0}\right) \quad (\text{eq. 2})$$

where  $k$  is the pseudo first-order rate constant,  $t$  is the time,  $C$  is the concentration of the pollutant, and  $C_0$  is the initial concentration of the pollutant. The linearized pseudo-first-order plots of  $\ln(C/C_0)$  versus time gives the apparent rate constant ( $k$ ). The corresponding pseudo first-order rate constants (Figure S5 and Table 2) also follows the previous trend, i.e. Ce/TiAP > TiAP > P25. Compared to other works using Ce surface-modified photocatalysts<sup>67,68</sup>, the present photocatalytic efficiency using Ce/TiAP was found to be significantly higher than, for instance, CeO<sub>2</sub> decorated bismuth molybdate (CeO<sub>2</sub>/Bi<sub>2</sub>MoO<sub>6</sub>) in the degradation of RB under UV light<sup>67</sup>. Indeed, Ce/TiAP degraded 94% of the RB in 10 min

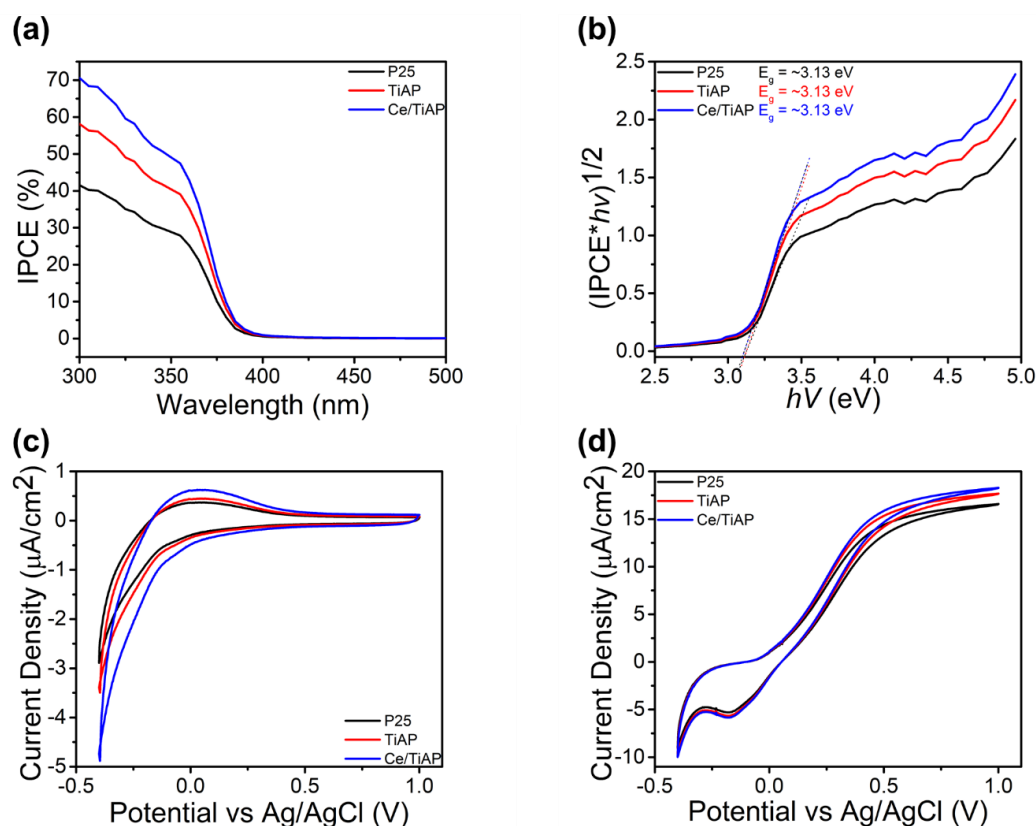


**Figure 7:** (a) IPCE% vs. wavelength, (b) energy bandgap from IPCE, (c) CV curves recorded in the dark, and (d) CV curves recorded under 360 nm light irradiation.

#### Photocatalytic degradation of Rhodamine B, phenol and caffeine

The photocatalytic degradation of environmentally relevant contaminants including Rhodamine B, phenol and caffeine was carried out using Ce/TiAP, TiAP and P25 under solar-like irradiation (Figure 8). In each degradation experiment, the photocatalytic efficiency of the TiO<sub>2</sub> samples was the following: Ce/TiAP > TiAP > P25. Indeed, Ce/TiAP samples led to 94 % RB degradation in 10 min and 67 % CAF degradation in 20 min under UVA light. Moreover, the mineralization was monitored for 2 h where 50 % and 84 % mineralization extent was observed for CAF and phenol, respectively (Figure 8). The

(Figure 8a) whereas CeO<sub>2</sub>/Bi<sub>2</sub>MoO<sub>6</sub> took 90 min to achieve similar degradation extent. In addition, repeated runs of photocatalytic degradation of RB, phenol and CAF using Ce/TiAP have been performed (Figure S6). The reproducibility after 4 cycles is satisfactory with almost a stable degradation efficiency of RB and a decrease of mineralization efficiency (for phenol and CAF) of less 2% per cycle.

**Table 2:** The pseudo-first-order rate constants ( $k$ ) of the photocatalytic degradation of Rhodamine B, Phenol and Caffeine); The indirect bandgap for P25, TiAP and Ce/TiAP samples calculated from DRS and IPCE.

Sample Name	Pollutant	Kinetic Constant ( $k$ ) ( $\text{min}^{-1}$ )	Indirect Optical Bandgap (DRS)	Indirect Electronic Bandgap (IPCE)
P25	Rhodamine B	0.083	3.09 eV	3.13 eV
	Phenol (mineralization)	0.005		
	Caffeine	0.036		
	Caffeine (mineralization)	0.004		
TiAP	Rhodamine B	0.121	3.25 eV	3.13 eV
	Phenol (mineralization)	0.011		
	Caffeine	0.040		
	Caffeine (mineralization)	0.004		
Ce/TiAP	Rhodamine B	0.289	3.25 eV	3.13 eV
	Phenol (mineralization)	0.015		
	Caffeine	0.053		
	Caffeine (mineralization)	0.006		

enhancement of photocatalytic efficiency since longer life-time of photo-generated species increases the probability to generate the primary ROS according to the chemical reactions in equations 3 and 4. The formation of these radical species is the base of the photocatalytic degradation of organic pollutants. In addition, the nanostructured Ce/TiAP particles (Figures 3 and Figure 4) along with their high active surface area (Table 1) are also crucial parameters for the photocatalytic efficiency. That leads to an increase of active sites where reactions take place since photocatalysis is a surface dependent process (Langmuir-Hinshelwood mechanism).



Furthermore, the main ROS generated by  $\text{TiO}_2$ -based photocatalytic systems are hydroxyl radicals<sup>69,70</sup>. Their generation under UVA light was first followed by fluorescence spectroscopy (Figure 9). It confirms the higher production rate of hydroxy-terephthalic acid in the presence of Ce/TiAP with a 5-fold increase compared to TiAP, with a concentration of 700 nM after 10 min. To further confirm the presence of  $\text{HO}^\bullet$  radicals, EPR measurements were performed. The UVA exposure of TiAP and Ce/TiAP dispersed in water in the

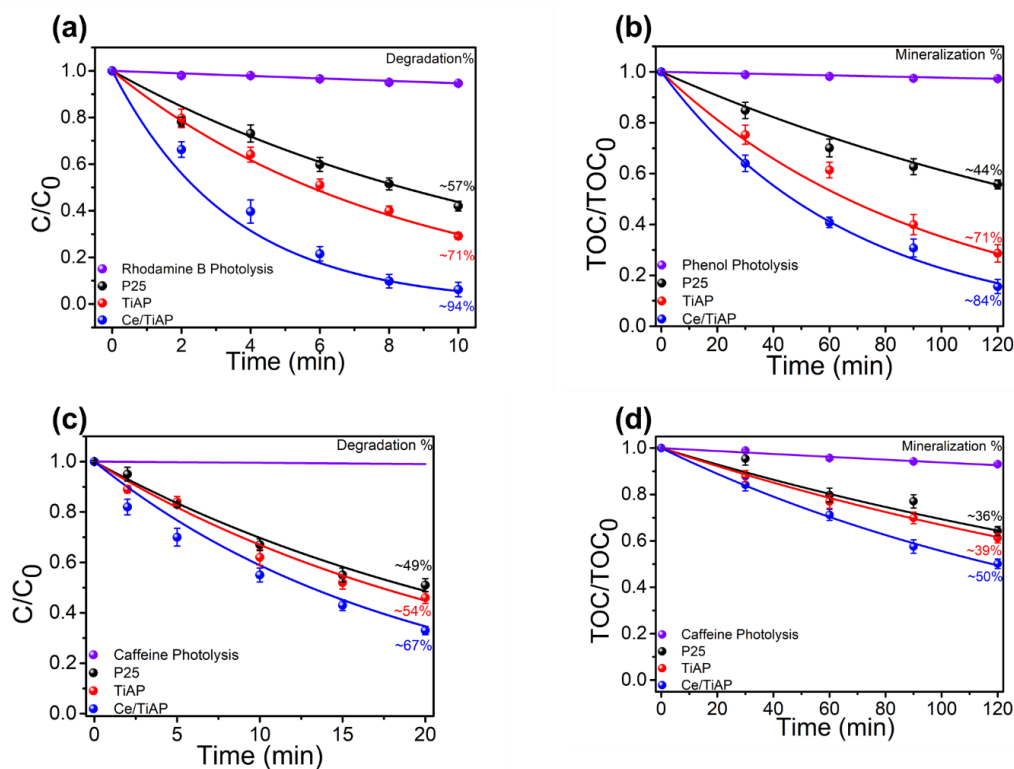


**Figure 8:** Photocatalytic Activity of Ce/TiAP (a) Rhodamine B, (b) phenol mineralization measured by total organic carbon content analyzer, (c) & (d) caffeine degradation by HPLC and mineralization measured by total organic carbon content analyzer.

The photocatalytic efficiency of the samples correlated with their morphological, structural, optical and photo-electrochemical properties. Indeed, the photo-electrochemical properties suggest the enhanced  $\text{e}^-/\text{h}^+$  separation in Ce/TiAP. The photocurrent density produced by Ce/TiAP (Figure S4) clearly exhibits enhanced charge transport while efficient photon to electron conversion (Figure 7a) is also observed for Ce/TiAP. The  $\text{e}^-/\text{h}^+$  pair separation is a key factor for the

presence of DMPO spin trap results in the immediate generation of typical four-line EPR signal (Figure 10a and Figure S7), characterized by the spin-Hamiltonian parameters fully compatible with  $^*\text{DMPO-OH}$  spin-adduct ( $a_N = 1.509 \text{ mT}$ ,  $a_H^\beta = 1.480 \text{ mT}$ ,  $a_{13C}(2 \times ^{13}\text{C}) = 0.768 \text{ mT}$ ,  $a_{13C} = 0.585 \text{ mT}$ ,  $a_{13C} = 0.465 \text{ mT}$ ;  $g = 2.0057$ )<sup>71-73</sup>. The  $^*\text{DMPO-OH}$  adduct may be generated in the photoactivated aqueous  $\text{TiO}_2$  suspensions via several alternative mechanisms, representing (i) genuine

trapping of HO• radicals by DMPO, (ii) rapid transformation of •DMPO-O<sub>2</sub>H and (iii) inverted spin-trapping <sup>72,73</sup>.

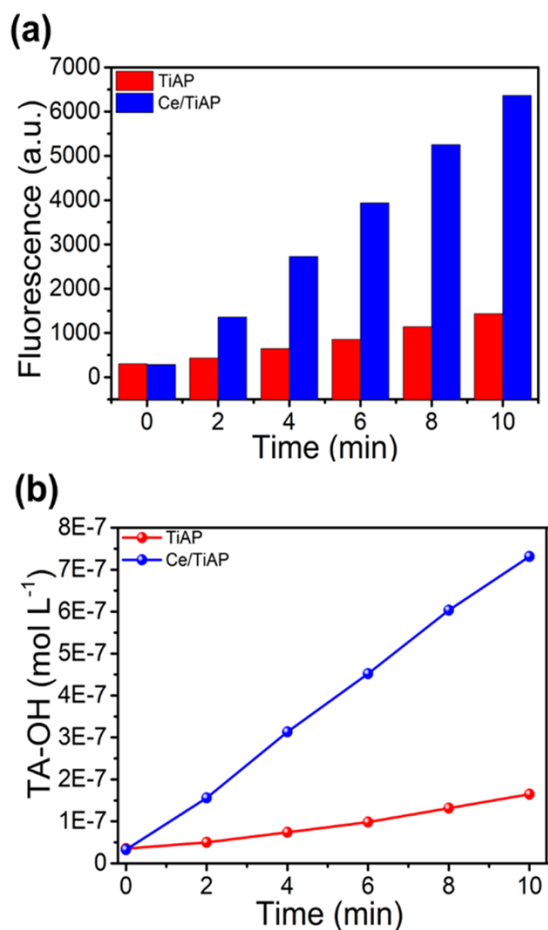


**Figure 9:** Dependence over time of (a) fluorescence and (b) concentration of hydroxy-terephthalic acid (TA-OH) produced during irradiation of TiAP and Ce/TiAP under UVA light.

Consequently, the analogous EPR spin trapping experiments were performed with BMPO, which represents a spin trapping agent suitable for the simultaneous detection of HO• and O<sub>2</sub><sup>•-</sup>/HO<sub>2</sub><sup>•</sup> radicals <sup>74-76</sup>. Figure 10b shows the normalized experimental and simulated EPR spectra obtained upon 180 s LED@365 nm exposure of aerated aqueous suspension of Ce/TiAP in the presence of BMPO. The experimental EPR spectrum was interpreted by the simulation analysis and the best fit evaluated corresponds to the superposition of two individual BMPO-adducts characterized by the following spin-Hamiltonian parameters and relative concentration: (i) •BMPO-OH(1) (conformer 1)  $a_N = 1.435$  mT,  $a_{H\beta} = 1.527$  mT,  $a_{H\gamma} = 0.066$  mT;  $g = 2.0057$ ; 29 %, and (ii) •BMPO-OH(2) (conformer 2)  $a_N = 1.415$  mT,  $a_{H\beta} = 1.263$  mT,  $a_{H\gamma} = 0.064$  mT;  $g = 2.0057$ ; 71 %. It should be noted here, that the EPR signals characteristic for the •BMPO-O<sub>2</sub>H(1) and •BMPO-O<sub>2</sub>H(2) conformers <sup>74-76</sup> were not detected upon LED@365 nm irradiation of aerated TiAP and Ce/TiAP suspensions. In addition, Ce/TiAP exhibited a shift in the band structure compared to TiAP (Figure 6), thus improving the generation of HO•. Indeed, O<sub>2</sub><sup>•-</sup>/HO<sub>2</sub><sup>•</sup> might also be generated in Ce/TiAP

systems and form in-situ H<sub>2</sub>O<sub>2</sub> which is subsequently transformed into HO• <sup>72</sup>. The radical scavenging experiments in presence of different radical scavengers further proved that HO• is the main primary ROS (Figures S8 and S9). Indeed, in presence of IPA, the photocatalytic degradation of organic pollutants is strongly inhibited. In the presence of AO and BQ, there is a less significant inhibition, thus confirming that hydroxyl radicals can be either produced from oxidation of hydroxyl anions (eq. 3) or by in-situ decomposition of H<sub>2</sub>O<sub>2</sub> (eqs. 4-6).

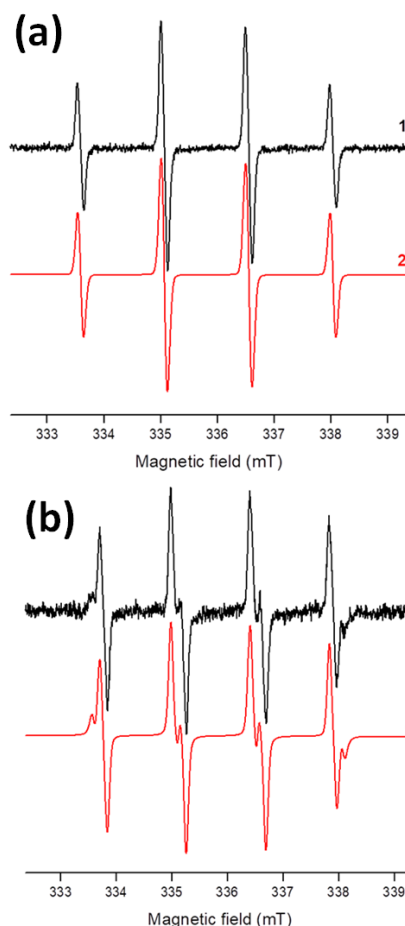
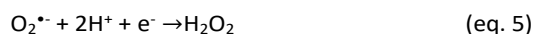


**Figure 10:** The normalized experimental (1) and simulated (2) EPR spectra obtained after 180 s exposure of aerated aqueous suspensions of Ce/TiAP in the presence of spin trapping agent: (a) DMPO; (b) BMPO. (LED@365 nm, irradiance 10 mW·cm<sup>-2</sup>; photocatalyst loading 0.2 mg·mL<sup>-1</sup>; c0(DMPO) = 0.04 M; c0(BMPO) = 0.02 M).

## Conclusions

The surface modification of TiO<sub>2</sub> aerogel powders by cerium ions was successfully performed for the first time. The effect of Ce surface-modification at the TiO<sub>2</sub> surface has led to an increase in active surface area compared to the TiAP sample. The photo-electrochemical measurements have exhibited the significantly better photocurrent density and IPCE of Ce/TiAP,

thus indirectly highlighting better e<sup>-</sup>/h<sup>+</sup> pair separation. In addition, although the energy bandgap of TiAP and Ce/TiAP is similar, the valence band of the surface-modified sample is shifted from 3.2 to 2.8 eV, thus improving the generation of ROS, especially hydroxyl radicals. All these detailed studies have provided insights into the improvement of photo-induced properties of Ce/TiAP, which have been correlated by the photo-degradation of different pollutants under UVA light. Indeed, Ce/TiAP has led to significantly better degradation and mineralization extents, thus these photocatalytic tests using different types of pollutant highlight the universality and the relevance of the Ce surface-modified TiO<sub>2</sub> aerogel powders and their promising use for environmental applications.

## Author Contributions (CRediT)

**Guru Karthikeyan Thirunavukkarasu:** Investigation - Methodology - Writing: original draft; **Olivier Monfort:** Conceptualization - Supervision - Methodology - Writing: original draft - Writing: review & editing; **Martin Motola:** Conceptualization - Investigation - Methodology - Writing: original draft - Writing: review & editing; **Monika Motlochová:** Investigation - Methodology - Writing: review & editing; **Maros Gregor:** Investigation; **Tomas Roch:** Investigation; **Maria Caplovicova:** Investigation - Methodology - Writing: original draft; **Aleksandra Y. Lavrikova:** Investigation; **Karol Hensel:** Investigation - Methodology; **Vlasta Brezova:** Investigation - Methodology - Writing: original draft; **Monika Jerigova:** Investigation; **Jan Subrt:** Conceptualization - Supervision - Writing: review & editing; **Gustav Plesch:** Conceptualization - Supervision - Writing: original draft - Writing: review & editing.

## Conflicts of interest

There are no conflicts to declare.

## Acknowledgements

Authors acknowledged the financial support provided by the Scientific Grant Agency of the Slovak Republic (projects VEGA 1/0712/18 and 1/0064/21) and the Slovak Research and Development Agency (project APVV-17-0324). Authors also thank prof. Marcello Brigante, Université Clermont Auvergne (France) for his help in the analysis of caffeine degradation, and Dr. Jan Gregus, Comenius University in Bratislava, Faculty of Mathematics Physics and Informatics for DRS measurements. This publication is also the result of the major project "Advancing University Capacity and Competence in Research, Development and Innovation" (ITMS project code: 313021X329) supported by Operational Programme Integrated Infrastructure and funded by the European Regional Development Fund.

## References

1 G. Tian, H. Fu, L. Jing and C. Tian, *Journal of Hazardous Materials*, 2009, **161**, 1122–1130.

- 2 S. Rasalingam, R. Peng and R. T. Koodali, *Journal of Nanomaterials*, 2014, **2014**, 1–42.
- 3 M. Patel, R. Kumar, K. Kishor, T. Mlsna, C. U. Pittman and D. Mohan, *Chem. Rev.*, 2019, **119**, 3510–3673.
- 4 T. Rasheed, M. Bilal, F. Nabeel, M. Adeel and H. M. N. Iqbal, *Environment International*, 2019, **122**, 52–66.
- 5 S. Ahmed, M. G. Rasul, W. N. Martens, R. Brown and M. A. Hashib, *Desalination*, 2010, **261**, 3–18.
- 6 J. Zhang, Y. Wu, M. Xing, S. A. K. Leghari and S. Sajjad, *Energy Environ. Sci.*, 2010, **3**, 715.
- 7 R. Daghrir, P. Drogui and D. Robert, *Ind. Eng. Chem. Res.*, 2013, **52**, 3581–3599.
- 8 M. Pawar, S. Topcu Sendoğdular and P. Gouma, *Journal of Nanomaterials*, 2018, **2018**, 1–13.
- 9 V. Etacheri, C. Di Valentin, J. Schneider, D. Bahnemann and S. C. Pillai, *Journal of Photochemistry and Photobiology C: Photochemistry Reviews*, 2015, **25**, 1–29.
- 10 G. Dagan and M. Tomkiewicz, *J. Phys. Chem.*, 1993, **97**, 12651–12655.
- 11 Z. Zhao, X. Jiao and D. Chen, *J. Mater. Chem.*, 2009, **19**, 3078.
- 12 S. R. Mukai, H. Nishihara, S. Shichi and H. Tamon, *Chem. Mater.*, 2004, **16**, 4987–4991.
- 13 V. Štengl, S. Bakardjieva, J. Šubrt and L. Szatmary, *Microporous and Mesoporous Materials*, 2006, **91**, 1–6.
- 14 B. Malinowska, J. Walendziewski, D. Robert, J. V. Weber and M. Stolarski, *International Journal of Photoenergy*, 2003, **5**, 147–152.
- 15 L. Chen, J. Zhu, Y.-M. Liu, Y. Cao, H.-X. Li, H.-Y. He, W.-L. Dai and K.-N. Fan, *Journal of Molecular Catalysis A: Chemical*, 2006, **255**, 260–268.
- 16 T. L. Thompson and J. T. Yates, *Chem. Rev.*, 2006, **106**, 4428–4453.
- 17 J. Schneider, M. Matsuoka, M. Takeuchi, J. Zhang, Y. Horiuchi, M. Anpo and D. W. Bahnemann, *Chem. Rev.*, 2014, **114**, 9919–9986.
- 18 J. Zhang, B. Tian, L. Wang, M. Xing and J. Lei, in *Photocatalysis*, Springer Singapore, Singapore, 2018, vol. 100, pp. 1–15.
- 19 Y.-C. Nah, I. Paramasivam and P. Schmuki, *Chem. Eur. J. of Chem. Phys.*, 2010, **11**, 2698–2713.
- 20 H. Park, Y. Park, W. Kim and W. Choi, *Journal of Photochemistry and Photobiology C: Photochemistry Reviews*, 2013, **15**, 1–20.
- 21 J. S. Jang, H. G. Kim and J. S. Lee, *Catalysis Today*, 2012, **185**, 270–277.
- 22 J. Moma and J. Baloyi, in *Photocatalysts - Applications and Attributes*, eds. S. Bahadar Khan and K. Akhtar, IntechOpen, 2019.
- 23 A.-W. Xu, Y. Gao and H.-Q. Liu, *Journal of Catalysis*, 2002, **207**, 151–157.
- 24 V. Đorđević, B. Milićević and M. D. Dramićanin, in *Titanium Dioxide*, ed. M. Janus, InTech, 2017.
- 25 S. Akshatha, S. Sreenivasa, L. Parashuram, V. U. Kumar, S. C. Sharma, H. Nagabhushana, S. Kumar and T. Maiyalagan, *Journal of Environmental Chemical Engineering*, 2019, **7**, 103053.
- 26 G. Bahmanrokh, C. Cazorla, S. S. Mofarah, R. Shahmiri, Y. Yao, I. Ismail, W.-F. Chen, P. Koshy and C. C. Sorrell, *Nanoscale*, 2020, **12**, 4916–4934.
- 27 Z. Shayegan, F. Haghghat and C.-S. Lee, *Chemical Engineering Journal*, 2020, **401**, 125932.
- 28 C. Fan, P. Xue and Y. Sun, *Journal of Rare Earths*, 2006, **24**, 309–313.
- 29 E. Wang, P. Zhang, Y. Chen, Z. Liu, T. He and Y. Cao, *J. Mater. Chem.*, 2012, **22**, 14443–14449.

- 30 M. Rochkind, S. Pasternak and Y. Paz, *Molecules*, 2014, **20**, 88–110.
- 31 C. Wang, T. Zeng, S. Zhu and C. Gu, *Applied Sciences*, 2019, **9**, 339.
- 32 F. Zhang, J. Zhao, T. Shen, H. Hidaka, E. Pelizzetti and N. Serpone, *Applied Catalysis B: Environmental*, 1998, **15**, 147–156.
- 33 X. Xiao, R. Hao, M. Liang, X. Zuo, J. Nan, L. Li and W. Zhang, *Journal of Hazardous Materials*, 2012, **233–234**, 122–130.
- 34 J. Šubrt, P. Pulišová, J. Boháček, P. Bezdička, E. Pližingrová, L. Volfová and J. Kupčík, *Materials Research Bulletin*, 2014, **49**, 405–412.
- 35 E. Pližingrová, L. Volfová, P. Svara, N. K. Labhsetwar, M. Klementová, L. Szatmáry and J. Šubrt, *Catalysis Today*, 2015, **240**, 107–113.
- 36 D. Kornbrust and T. Barfknecht, *Environmental Mutagenesis*, 1985, **7**, 101–120.
- 37 D. B. McGregor, A. G. Brown, S. Howgate, D. McBride, C. Riach, W. J. Caspary and J. H. Carver, *Environmental and Molecular Mutagenesis*, 1991, **17**, 196–219.
- 38 S. D. Richardson, C. S. Willson and K. A. Rusch, *Groundwater*, 2004, **42**, 678–688.
- 39 A. Elhalil, R. Elmoubarki, M. Farnane, A. Machrouhi, M. Sadiq, F. Z. Mahjoubi, S. Qourzal and N. Barka, *Environmental Nanotechnology, Monitoring & Management*, 2018, **10**, 63–72.
- 40 Q. Lu, W. Gao, J. Du, L. Zhou and Y. Lian, *J. Agric. Food Chem.*, 2012, **60**, 4773–4778.
- 41 F. Qi, W. Chu and B. Xu, *Applied Catalysis B: Environmental*, 2013, **134–135**, 324–332.
- 42 W. W. Anku, M. A. Mamo and P. P. Govender, in *Phenolic Compounds - Natural Sources, Importance and Applications*, eds. M. Soto-Hernández, M. Palma-Tenango and M. del R. Garcia-Mateos, InTech, 2017.
- 43 M. O. Aremu, A. O. Arinkoola, I. A. Olowonyo and K. K. Salam, *Heliyon*, 2020, **6**, e04492.
- 44 S. Brunauer, P. H. Emmett and E. Teller, *J. Am. Chem. Soc.*, 1938, **60**, 309–319.
- 45 E. P. Barrett, L. G. Joyner and P. P. Halenda, *J. Am. Chem. Soc.*, 1951, **73**, 373–380.
- 46 M. Baudys, M. Zlámál, J. Krýsa, J. Jirkovský and P. Kluson, *React Kinet Mech Cat*, 2012, **106**, 297–311.
- 47 S. Kanazawa, T. Furuki, T. Nakaji, S. Akamine and R. Ichiki, *J. Phys.: Conf. Ser.*, 2013, **418**, 012102.
- 48 K. Bubacz, E. Kusiak-Nejman, B. Tryba and A. W. Morawski, *Journal of Photochemistry and Photobiology A: Chemistry*, 2013, **261**, 7–11.
- 49 S. Stoll and A. Schweiger, *Journal of Magnetic Resonance*, 2006, **178**, 42–55.
- 50 U. Holzwarth and N. Gibson, *Nature Nanotech*, 2011, **6**, 534–534.
- 51 E. Pližingrová, M. Klementová, P. Bezdička, J. Boháček, Z. Barbieriková, D. Dvoranová, M. Mazúr, J. Krýsa, J. Šubrt and V. Brezová, *Catalysis Today*, 2017, **281**, 165–180.
- 52 H. Izutsu, P. K. Nair and F. Mizukami, *J. Mater. Chem.*, 1997, **7**, 855–856.
- 53 K. R. N. Pai, G. S. Anjusree, T. G. Deepak, D. Subash, S. V. Nair and A. S. Nair, *RSC Adv.*, 2014, **4**, 36821–36827.
- 54 Y. Zhang, A. H. Yuwono, J. Wang and J. Li, *J. Phys. Chem. C*, 2009, **113**, 21406–21412.
- 55 Md. K. Hossain, A. R. Koirala, U. S. Akhtar, M. K. Song and K. B. Yoon, *Chem. Mater.*, 2015, **27**, 6550–6557.
- 56 J. Liu, D. L. McCarthy, M. J. Cowan, E. A. Obuya, J. B. DeCoste, K. H. Skorenko, L. Tong, S. M. Boyer, W. E. Bernier and W. E. Jones Jr., *Applied Catalysis B: Environmental*, 2016, **187**, 154–162.
- 57 W. Fu, G. Li, Y. Wang, S. Zeng, Z. Yan, J. Wang, S. Xin, L. Zhang, S. Wu and Z. Zhang, *Chem. Commun.*, 2018, **54**, 58–61.
- 58 L. Sheng, T. Liao, L. Kou and Z. Sun, *Materials Today Energy*, 2017, **3**, 32–39.
- 59 M. Velický and P. S. Toth, *Applied Materials Today*, 2017, **8**, 68–103.
- 60 S. H. Mir, V. K. Yadav and J. K. Singh, *ACS Omega*, 2020, **5**, 14203–14211.
- 61 M. V. Martin, O. M. Alfano and M. L. Satuf, *Journal of Environmental Chemical Engineering*, 2019, **7**, 103478.
- 62 Y. Liu, P. Fang, Y. Cheng, Y. Gao, F. Chen, Z. Liu and Y. Dai, *Chemical Engineering Journal*, 2013, **219**, 478–485.
- 63 M. Motola, H. Sopha, M. Krbal, L. Hromádka, Z. O. Zmrhalová, G. Plesch and J. M. Macak, *Electrochemistry Communications*, 2018, **97**, 1–5.
- 64 M. Motola, L. Hromádka, J. Prikryl, H. Sopha, M. Krbal and J. M. Macak, *Electrochimica Acta*, 2020, **352**, 136479.
- 65 R. Beranek, H. Tsuchiya, T. Sugishima, J. M. Macak, L. Taveira, S. Fujimoto, H. Kisch and P. Schmuki, *Appl. Phys. Lett.*, 2005, **87**, 243114.
- 66 M. T. Laciste, M. D. G. de Luna, N. C. Tolosa and M.-C. Lu, *Chemosphere*, 2020, **246**, 125763.
- 67 S. Li, S. Hu, W. Jiang, Y. Liu, Y. Zhou, J. Liu and Z. Wang, *Journal of Colloid and Interface Science*, 2018, **530**, 171–178.
- 68 L. Zhu, H. Li, P. Xia, Z. Liu and D. Xiong, *ACS Appl. Mater. Interfaces*, 2018, **10**, 39679–39687.
- 69 C. Turchi, *Journal of Catalysis*, 1990, **122**, 178–192.
- 70 J. Zhang and Y. Nosaka, *J. Phys. Chem. C*, 2013, **117**, 1383–1391.
- 71 G. R. Buettner, *Free Radical Biology and Medicine*, 1987, **3**, 259–303.
- 72 D. Dvoranová, Z. Barbieriková and V. Brezová, *Molecules*, 2014, **19**, 17279–17304.
- 73 Z. Barbieriková, D. Dvoranová, M.-V. Sofianou, C. Trapalis and V. Brezová, *Journal of Catalysis*, 2015, **331**, 39–48.
- 74 H. Zhao, J. Joseph, H. Zhang, H. Karoui and B. Kalyanaraman, *Free Radical Biology and Medicine*, 2001, **31**, 599–606.
- 75 A. Misak, L. Kurakova, E. Goffa, V. Brezova, M. Grman, E. Ondriasova, M. Chovanec and K. Ondrias, *Molecules*, 2019, **24**, 1148.
- 76 A. Misak, V. Brezova, M. Grman, L. Tomasova, M. Chovanec and K. Ondrias, *Antioxidants*, 2020, **9**, 918.

## Ce ions surface-modified TiO<sub>2</sub> aerogel powders: a comprehensive study of their excellent photocatalytic efficiency in organic pollutants removal

Guru Karthikeyan Thirunavukkarasu,<sup>a</sup> Olivier Monfort,<sup>a,\*</sup> Martin Motola,<sup>a</sup> Monika Motlochová,<sup>b</sup> Maroš Gregor,<sup>c</sup> Tomáš Roch,<sup>c</sup> Maria Čaplovicová,<sup>d</sup> Aleksandra Y. Lavrikova,<sup>e</sup> Karol Hensel,<sup>e</sup> Vlasta Brezová,<sup>f</sup> Monika Jerigová,<sup>g,h</sup> Ján Šubrt,<sup>b</sup> Gustáv Plesch<sup>a</sup>

### Electronic Supplementary Information

<sup>a</sup> Department of Inorganic Chemistry, Faculty of Natural Sciences, Comenius University in Bratislava, Ilkovicova 6, Mlynska Dolina, 842 15 Bratislava, Slovakia

<sup>b</sup> Institute of Inorganic Chemistry, Czech Academy of Sciences, Husinec-Rez c.p. 1001, 250 68 Rez, Czechia

<sup>c</sup> Department of Experiment Physics, Faculty of Mathematics, Physics and Informatics, Comenius University in Bratislava, Mlynska Dolina, 842 48 Bratislava, Slovakia

<sup>d</sup> STU Center for Nanodiagnostics, Slovak University of Technology in Bratislava, Vazovova 5, 812 43 Bratislava, Slovakia

<sup>e</sup> Division of Environmental Physics, Faculty of Mathematics, Physics and Informatics, Comenius University in Bratislava, Mlynska Dolina, 84248, Bratislava, Slovakia

<sup>f</sup> Institute of Physical Chemistry and Chemical Physics, Faculty of Chemistry and Food technology, Slovak University of Technology in Bratislava, Radlinskeho 9, 812 37 Bratislava, Slovakia

<sup>g</sup> International Laser Centre, Ilkovicova 3, 842 48 Bratislava, Slovakia

<sup>h</sup> Department of Physical and Theoretical Chemistry, Faculty of Natural Sciences, Comenius University in Bratislava, Ilkovicova 6, Mlynska dolina, 842 15 Bratislava, Slovakia

\* Corresponding author: monfort1@uniba.sk (email), +421(0)290142141 (phone)

**Calculation of percentage of anatase phase present in P25 sample:**

The P25 samples consist of ~82% of anatase phase, which is calculated using the formula <sup>1</sup>:

$$W_A = \frac{1}{1 + 1.26 \left(\frac{I_R}{I_A}\right)}$$

where,  $I_R$  and  $I_A$  is the strongest intensity of the rutile (110) and anatase (101) diffraction peak, respectively.

**Table S1:** Summary of Ce modified TiO<sub>2</sub> for photocatalytic application.

Material	Synthesis Technique	Ce Dopant Concentration	Bandgap (eV)	Type of Pollutant	Degradation %	Ref.
Ce <sup>3+</sup> -TiO <sub>2</sub> catalysts	Sol-gel	0.7% atomic ratio (Ce/Ti)	Not calculated. But adsorption increased in the 400-500 nm region	<ul style="list-style-type: none"> <li>• 2-mercaptobenzothiazole</li> <li>• Visible Light</li> <li>• 1.1 h</li> </ul>	100	<sup>2</sup>
Ce-TiO <sub>2</sub>	Sol-gel	0.4wt% (Ce/TiO <sub>2</sub> )	Not calculated. But adsorption increased in the 400-500 nm region	<ul style="list-style-type: none"> <li>• Phenol</li> <li>• UV light</li> <li>• 3 h</li> </ul>	100	<sup>3</sup>
Ce <sup>3+</sup> doped TiO <sub>2</sub>	Precipitation	1.47wt% (EDX)	3.15	<ul style="list-style-type: none"> <li>• Orange II dye</li> <li>• 400 nm</li> <li>• 0.5 h</li> </ul>	~40	<sup>4</sup>
Mesoporous Ce/TiO <sub>2</sub>	Sol-gel	5 mol%	Not calculated. But adsorption increased in the 400-500 nm region	<ul style="list-style-type: none"> <li>• Methylene blue (MB)</li> <li>• Visible light</li> <li>• 1 h</li> </ul>	100	<sup>5</sup>
Cerium-doped SiO <sub>2</sub> /TiO <sub>2</sub> nanofibers	Sol-gel and electrospinning	0.2% molar ratio (Ce/Ti)	Not calculated. But adsorption increased in the 400-500 nm region	<ul style="list-style-type: none"> <li>• Methylene blue (MB)</li> <li>• Simulated sunlight</li> <li>• 2 h</li> </ul>	~80	<sup>6</sup>
Ce doped TiO <sub>2</sub> nanosheets	Hydrothermal	0.5% molar ratio	~3	<ul style="list-style-type: none"> <li>• Rhodamine B</li> <li>• UV-Visible light</li> <li>• 1 h</li> </ul>	~90	<sup>7</sup>
Ce- and S-co-doped TiO <sub>2</sub>	Sol-gel	0.04 g (Ce(NO <sub>3</sub> ) <sub>3</sub> .6H <sub>2</sub> O)	2.66	<ul style="list-style-type: none"> <li>• Acid Orange 7 (AO-7)</li> <li>• Visible Light</li> <li>• 5 h</li> </ul>	100	<sup>8</sup>
Ce/N co-doped TiO <sub>2</sub>	Hydrothermal	0.05 g (Ce(NO <sub>3</sub> ) <sub>3</sub> .6H <sub>2</sub> O)	1.8	<ul style="list-style-type: none"> <li>• Acid Orange 7 (AO-7)</li> <li>• Visible Light</li> <li>• 5 h</li> </ul>	100	<sup>9</sup>
Sn/Ce co-doped TiO <sub>2</sub>	Sol-gel	2 mol%	3.02	<ul style="list-style-type: none"> <li>• Methylene blue (MB)</li> <li>• Solar light</li> <li>• 2 h</li> </ul>	~80	<sup>10</sup>
Ce-TiO <sub>2</sub> P25	Hydrothermal	0.29 mol% (Ce/TiO <sub>2</sub> )	3.25	<ul style="list-style-type: none"> <li>• Methylene blue (MB)</li> <li>• Visible light</li> <li>• 2.4 h</li> </ul>	~96	<sup>11</sup>
Ti <sup>3+</sup> -TiO <sub>2</sub> /Ce <sup>3+</sup> -CeO <sub>2</sub> nanosheet	Hydrothermal	1.56 at % (XPS)	2.7	<ul style="list-style-type: none"> <li>• Methyl orange (MO) and methylene blue (MB)</li> <li>• Visible light</li> <li>• 3 h</li> </ul>	~99	<sup>12</sup>
In <sub>0.2</sub> - Ce <sub>0.2</sub> /TiO <sub>2</sub> aerogels	Sol-gel	0.45 at%	2.84	<ul style="list-style-type: none"> <li>• Rhodamine B</li> <li>• Visible</li> <li>• 1.5 h</li> </ul>	~96	<sup>13</sup>
Ce doped TiO <sub>2</sub>	Sol-gel	0.5wt%	3.06	<ul style="list-style-type: none"> <li>• Caffeine</li> <li>• Visible light</li> <li>• 2 h</li> </ul>	~30	<sup>14</sup>
Ce-TiO <sub>2</sub> P25	Hydrothermal	0.5wt% (Ce/Ti)	2.4	<ul style="list-style-type: none"> <li>• Methylene blue (MB)</li> <li>• Visible light</li> <li>• 1.3 h</li> </ul>	~90	<sup>15</sup>
Ce-doped anatase TiO <sub>2</sub>	Sol-gel	0.1 mol%	3.31	<ul style="list-style-type: none"> <li>• Methylene blue (MB)</li> <li>• UV light</li> <li>• 24 h min</li> </ul>	~90	<sup>16</sup>

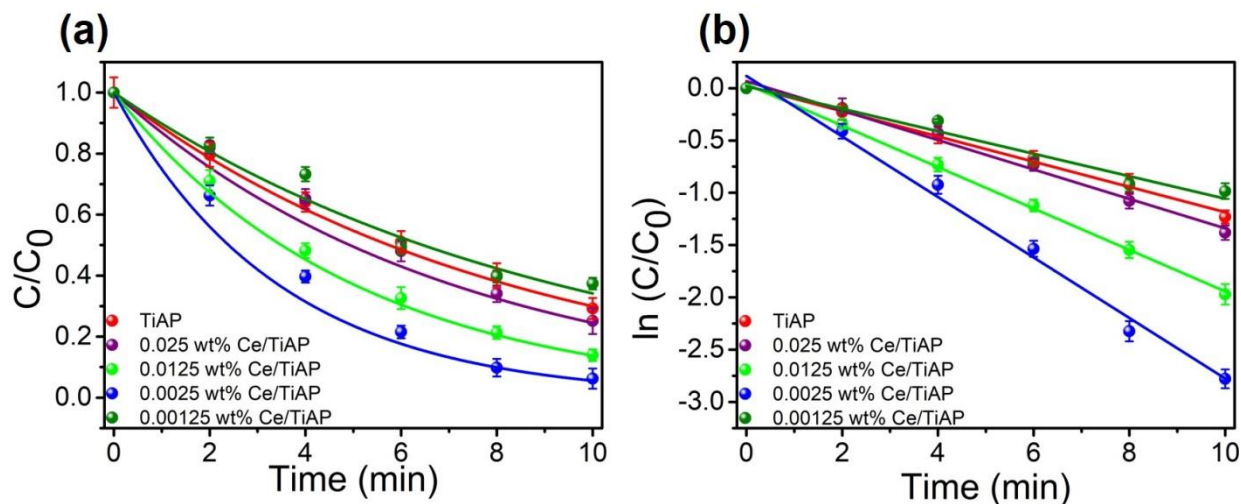


**Figure S1:** Influence of cerium ions surface-modification content on TiAP upon the photocatalytic efficiency in Rhodamine B decolorization under UVA light.

**Table S2:** The tabulation of photocatalytic activity rate ( $k$ ) and degradation % of rhodamine B under UVA light with different concentration of cerium surface modification on TiAP.

Sample	Photocatalytic activity rate ( $k$ ) $\text{min}^{-1}$	Degradation %
TiAP	0.121	~71
0.025 wt% Ce/TiAP	0.141	~75
0.0125 wt% Ce/TiAP	0.198	~86
0.0025 wt% Ce/TiAP	0.289	~94
0.00125 wt% Ce/TiAP	0.107	~63

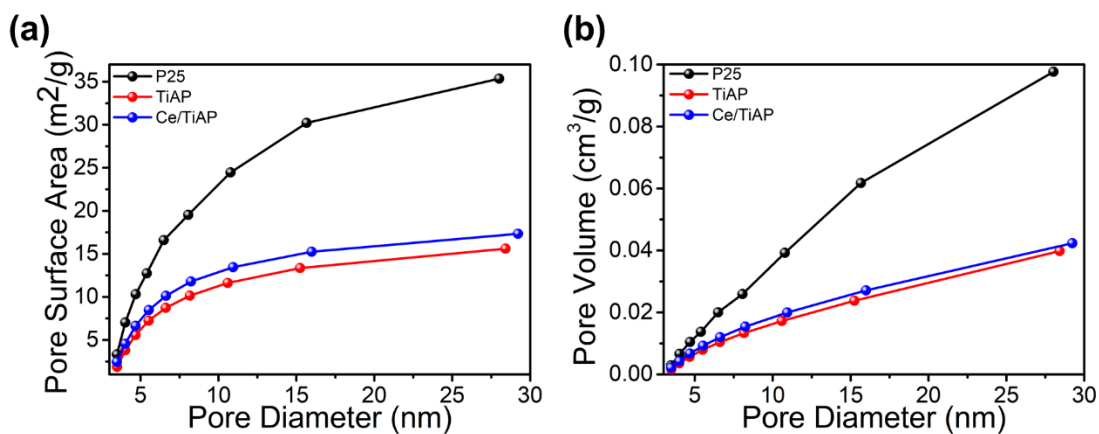


**Figure S2:** BET measurements of (a) Pore surface area and (b) pore volume respectively.

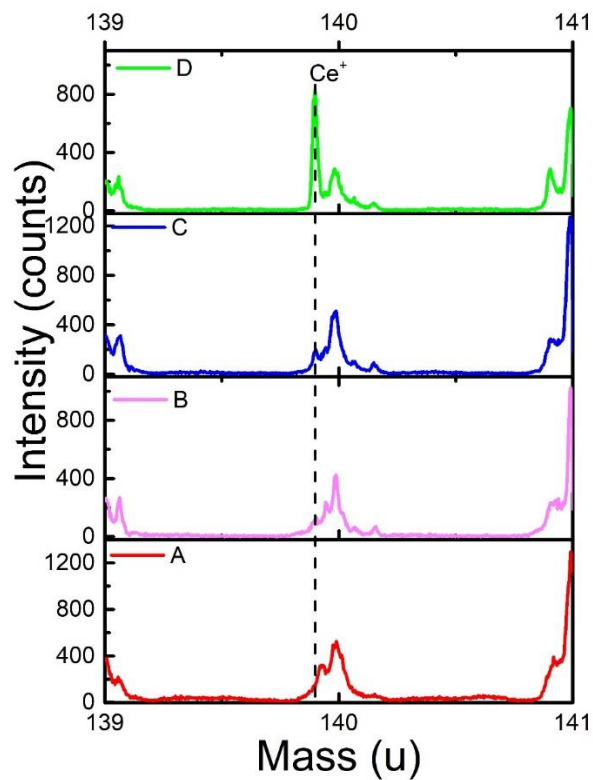


**Figure S3:** SIMS based detection of Ce in Ce/TiAP (A: Pristine TiAP, B: 0.00125 wt% Ce/TiAP, C: 0.0025 wt% Ce/TiAP and D: 0.0125 wt% Ce/TiAP). Ce<sup>+</sup> ion peak was identified at 139.9 mu (dash line).

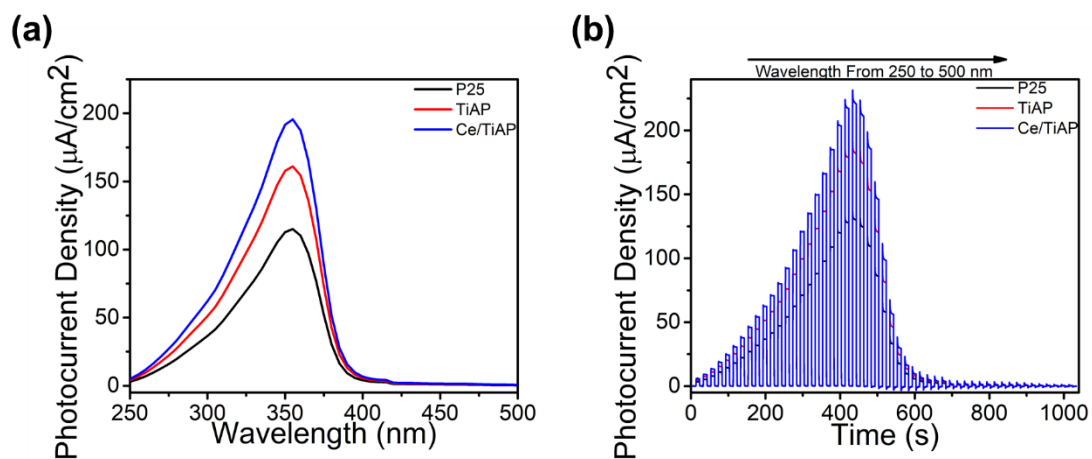


**Figure S4:** (a) Photocurrent densities of P25, TiAP and Ce/TiAP with (b) the corresponding transient current measured at 0.4 V<sub>vs</sub> Ag/AgCl in an aqueous 0.1 M Na<sub>2</sub>SO<sub>4</sub> solution in the spectral range from 300 nm to 500 nm.

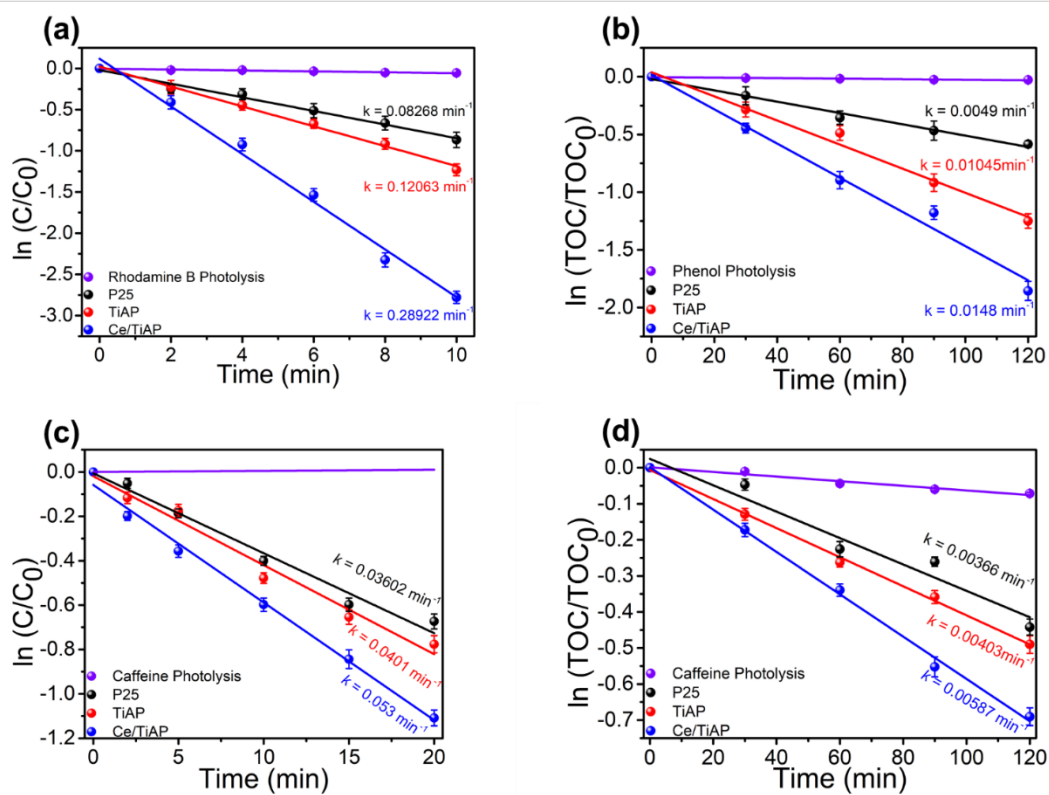


**Figure S5:** The linearized pseudo-first-order plots of  $\ln(C/C_0)$  versus time (a) Rhodamine B, (b) Phenol mineralization measured by total organic carbon content analyzer, (c) & (d) Caffeine degradation by HPLC and mineralization measured by total organic carbon content analyzer.

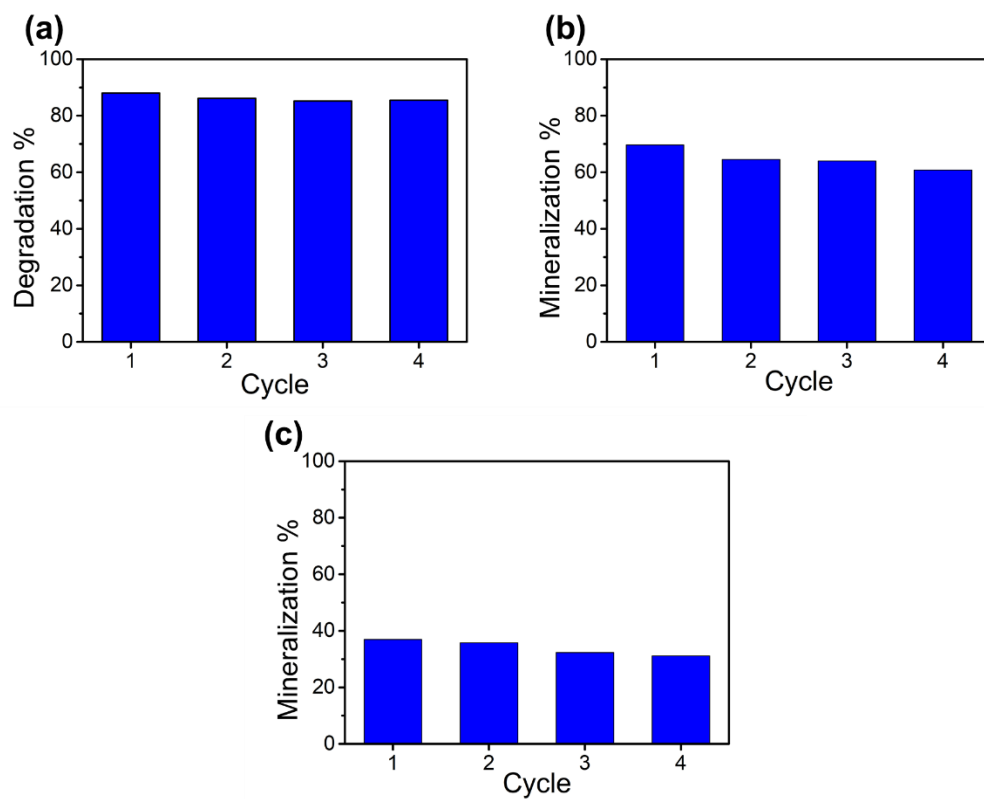


**Figure S6:** Repeated runs (4 cycles) using Ce/TiAP under UVA irradiation for the photocatalytic degradation of (a) Rhodamine B ( $C/C_0$ ), (b) Phenol (TOC), (c) Caffeine (TOC).

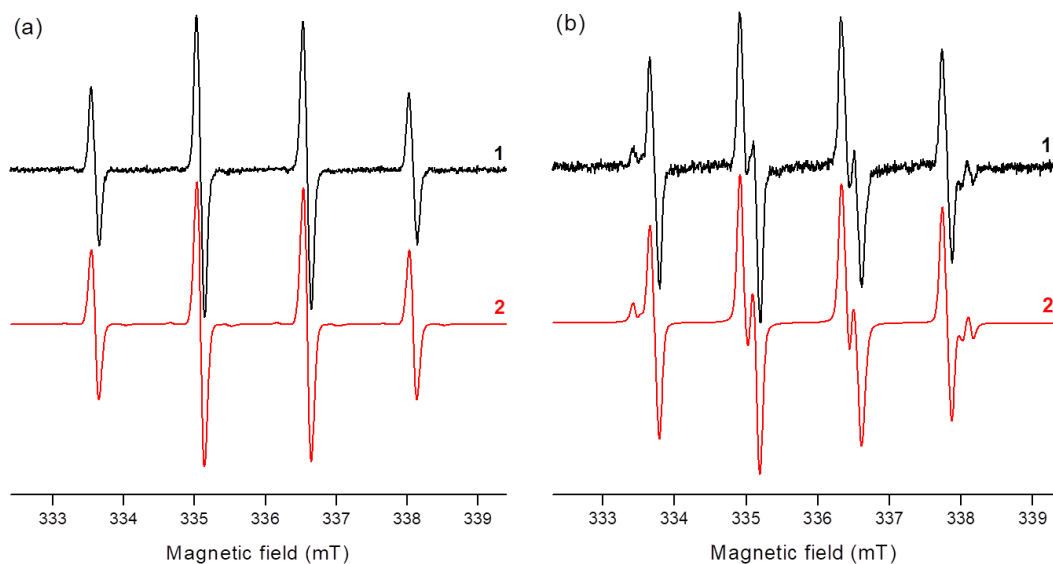


**Figure S7:** The normalized experimental (1) and simulated (2) EPR spectra obtained after 180-s exposure of aerated aqueous suspensions of TiAP in the presence of spin trapping agent: (a) DMPO; (b) BMPO. (LED@365 nm, irradiance  $10 \text{ mW cm}^{-2}$ ;  $\text{TiO}_2$  loading  $0.2 \text{ mg mL}^{-1}$ ;  $c_0(\text{DMPO}) = 0.04 \text{ M}$ ;  $c_0(\text{BMPO}) = 0.02 \text{ M}$ ).

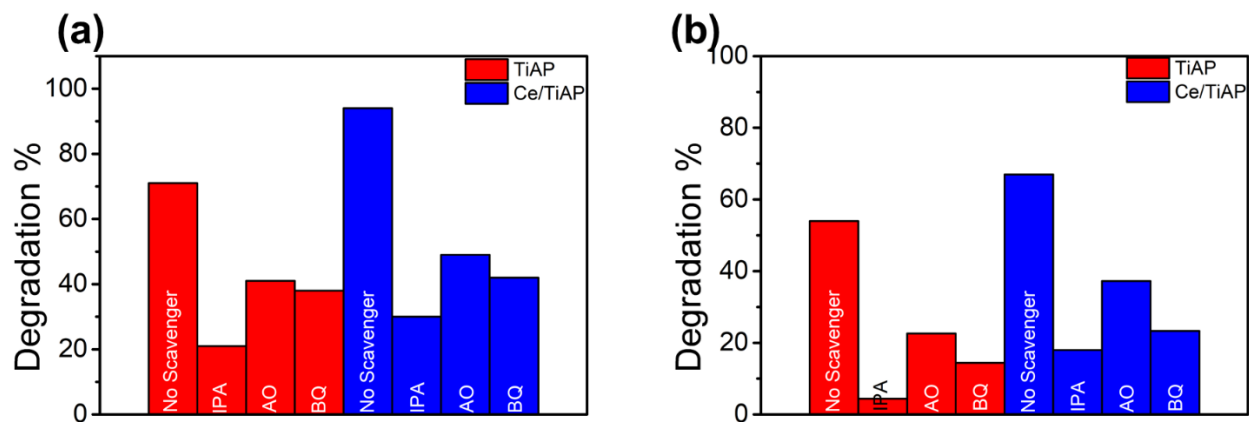


**Figure S8:** Free radical quenching of TiAP and Ce/TiAP using the isopropyl alcohol (IPA), ammonium oxalate (AO), benzoquinone (BQ) as scavengers (a) Rhodamine B and (b) caffeine.

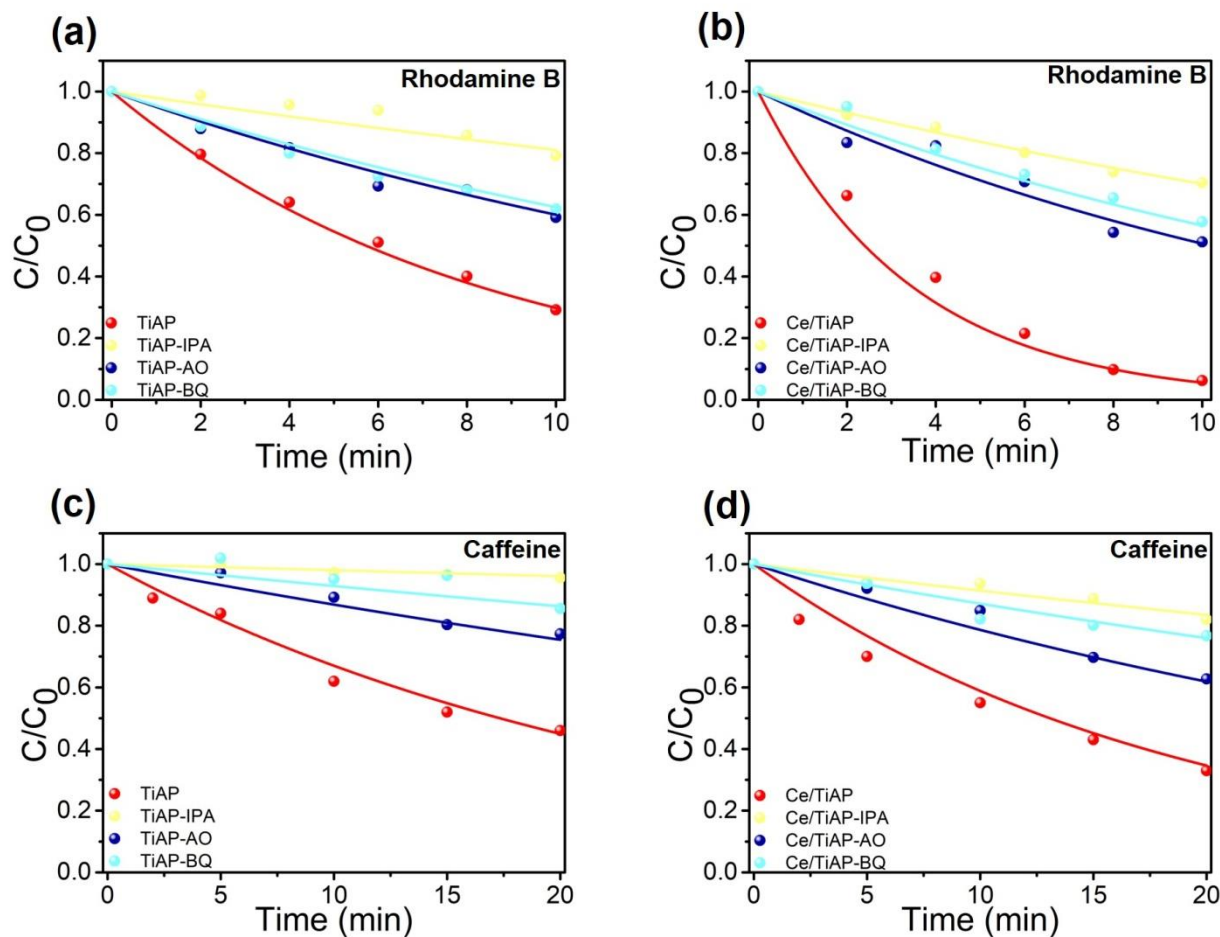


**Figure S9:** Degradation curves of (a) and (b) Rhodamine B and (c) and (d) Caffeine using TiAP and Ce/TiAPn respectively, under UVA irradiation.

## References

- 1 R. A. Spurr and Howard. Myers, *Anal. Chem.*, 1957, **29**, 760–762.
- 2 F. B. Li, X. Z. Li, M. F. Hou, K. W. Cheah and W. C. H. Choy, *Applied Catalysis A: General*, 2005, **285**, 181–189.
- 3 C. Fan, P. Xue and Y. Sun, *Journal of Rare Earths*, 2006, **24**, 309–313.
- 4 V. Štengl, S. Bakardjieva and N. Murafa, *Materials Chemistry and Physics*, 2009, **114**, 217–226.
- 5 N. Aman, P. K. Satapathy, T. Mishra, M. Mahato and N. N. Das, *Materials Research Bulletin*, 2012, **47**, 179–183.
- 6 Y. Liu, H. Yu, Z. Lv, S. Zhan, J. Yang, X. Peng, Y. Ren and X. Wu, *Journal of Environmental Sciences*, 2012, **24**, 1867–1875.
- 7 Y. Liu, P. Fang, Y. Cheng, Y. Gao, F. Chen, Z. Liu and Y. Dai, *Chemical Engineering Journal*, 2013, **219**, 478–485.
- 8 M. Nasir, Z. Xi, M. Xing, J. Zhang, F. Chen, B. Tian and S. Bagwasi, *J. Phys. Chem. C*, 2013, **117**, 9520–9528.
- 9 M. Nasir, S. Bagwasi, Y. Jiao, F. Chen, B. Tian and J. Zhang, *Chemical Engineering Journal*, 2014, **236**, 388–397.
- 10 M. Aljani and B. K. Kaleji, *Opt Quant Electron*, 2017, **49**, 34.
- 11 G. B. Vieira, H. J. José, M. Peterson, V. Z. Baldissarelli, P. Alvarez and R. de Fátima Peralta Muniz Moreira, *Journal of Photochemistry and Photobiology A: Chemistry*, 2018, **353**, 325–336.
- 12 Z. Xiu, Z. Xing, Z. Li, X. Wu, X. Yan, M. Hu, Y. Cao, S. Yang and W. Zhou, *Materials Research Bulletin*, 2018, **100**, 191–197.
- 13 R.-R. Zheng, T.-T. Li and H. Yu, *Global Challenges*, 2018, **2**, 1700118.
- 14 V. O. Ndalankulu, S. Maddila and S. B. Jonnalagadda, *Can. J. Chem.*, 2019, **97**, 672–681.
- 15 G. B. Vieira, G. Scaratti, F. S. Rodembusch, S. M. De Amorim, M. Peterson, G. L. Puma and R. D. F. P. M. Moreira, *Environmental Technology*, 2019, 1–15.
- 16 G. Bahmanrokh, C. Cazorla, S. S. Mofarah, R. Shahmiri, Y. Yao, I. Ismail, W.-F. Chen, P. Koshy and C. C. Sorrell, *Nanoscale*, 2020, **12**, 4916–4934.